RSC Advances

REVIEW

View Article Online
View Journal | View Issue

Cite this: *RSC Adv.*, 2021, **11**, 26855

Recent advances in bismuth oxyhalide photocatalysts for degradation of organic pollutants in wastewater†

Yang Li,[a] Haiyan Jiang,[b] Xu Wang,[a] Xiaodong Hong*[c] and Bing Liang[d]

Photocatalysis has been considered as an environmental-friendly strategy for degradation of organic pollutants to the nontoxic products of H_2O and CO_2. Compared to metal oxide semiconductors, BiOX (X = Cl, Br and I) photocatalysts exhibit some advantages, such as, unique layered structure, good chemical stability and superior photocatalytic activity. This review provides an overview on the controllable synthesis of BiOX-based photocatalysts and their application in photodegradation of organic pollutants. Firstly, the controllable synthesis of BiOX is introduced, including hydrothermal, solvothermal, hydrolysis, precipitation, two-phase methods, ultrasonic/microwave-assisted methods, and physical methods. Then, the doping and surface modification of BiOX are summarized, including non-metal doping, metal doping, dual doping, and the modification by introducing surface terminations or carriers. In addition, the heterojunctions of BiOX/BiOY and BiOX/$Bi_mO_nX_z$ are introduced. At last, the promising research trends of BiOX-based photocatalysts are put forward. The main purpose is providing practical guidelines for developing high-performance BiOX photocatalysts.

Received 30th July 2021
Accepted 2nd August 2021

DOI: 10.1039/d1ra05796k

rsc.li/rsc-advances

1. Introduction

The rapid development of modern industries causes environmental pollution, including air pollution, soil pollution and water pollution, which have been receiving much more attention in recent years. Water is a precious resource for the survival of animals and humans. Therefore, the treatment of water pollutants is an urgent task for the technicians and researchers. Among the strategies for solving wastewater pollution, photocatalysis is considered as an environmental-friendly method to obtain nontoxic degradation products. Under the irradiation of visible light or UV light, oxygen in the air is directly used as oxidant under normal reaction conditions, and organic pollutants in wastewater can be degraded into H_2O and CO_2, with no secondary pollutants. Moreover, the semiconductor photocatalysts have stable chemical properties, low cost, strong redox, and long service life.[1,2] Therefore, photocatalysis is particularly suitable for the purification of wastewater containing organic matter. Photocatalysis technique has been adopted as an effective strategy for degrading various organic contaminants, including antibiotics, organic dyes, organic acids, amines or phenols, and so on. Nowadays, developing high-performance photocatalysts has become a research hotspot in the photocatalysis field. Various metal oxide semiconductors, including TiO_2, SnO_2, ZnO, bismuth oxychloride (BiOX) have been synthesized and widely applied for the wastewater treatment.[3–5] Compared to traditional metal oxides, BiOX (X = Cl, Br, I) has some advantages,[6–8] such as, chemical stability, unique layered structure, easy preparation, and superior photocatalytic activity. In the unique lamellar structure of BiOX, the $[Bi_2O_2]$ layer is interleaved by X_2^{2-} slabs, and Bi–O and Bi–X bonds are connected by strong covalent bonding and weak Van der Waals interactions.[9] The band gap of BiOX decides the light absorption range. As shown in Fig. 1a, BiOCl has a broad band gap of ~3.3 eV, and exhibits a strong UV light absorption capability. Compared to BiOCl, BiOBr and BiOI have a low band gap of ~2.64 eV and ~1.77 eV, which enable them a strong visible light activity. The light absorption capability decides the photocatalytic activity of BiOX. Under the irradiation of light, when the absorbed light energy is greater than or equal to the energy gap of semiconductors, the electrons in the valence band (VB) can be excited and transferred to the conduction band (CB), leaving relatively stable holes in the VB, then electron–hole pairs are generated. During a photocatalytic reaction process, the electrons and holes participate in the redox reaction for degradation of organic pollutants. Due to the recombination of electrons and holes, the photocatalytic efficiency of semiconductors will be decreased. Therefore, the reduction of band

[a]College of Materials Science and Engineering, Liaoning Technical University, Fuxin 123000, China
[b]Basic Department, Liaoning Institute of Science and Technology, Benxi, 117004, China
[c]School of Materials Science and Hydrogen Energy, Foshan University, Foshan 528000, China. E-mail: hongxiaodong@lntu.edu.cn
[d]College of Materials Science and Engineering, Shenyang University of Chemical Technology, Shenyang 110142, China

† Electronic supplementary information (ESI) available. See DOI: 10.1039/d1ra05796k

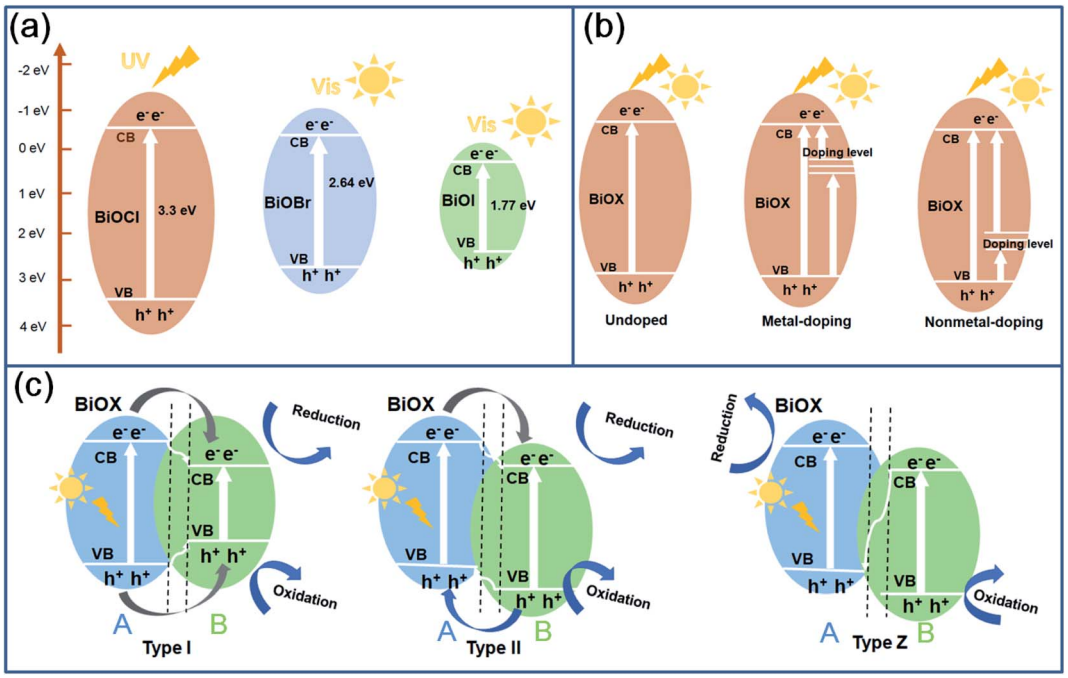

Fig. 1 The band gap structure of BiOCl, BiOBr and BiOI (a), the effect of heteroatom doping of BiOX (b) and construction of different types of BiOX heterojunctions (c).

gap energy and inhibiting the recombination of electrons and holes are the major strategies for improving the photocatalytic efficiency of BiOX.

In order to reduce the band gap of BiOX, the microstructure design, heteroatom doping and the construction of heterojunction are the effective measures.[10] In the field of microstructure design, the control of morphology and surface defects including oxygen vacancies and exposed (001) facets have been widely reported. From the relationship between heteroatom doping and band gap structure in Fig. 1b, metal-doping can be adopted for adjusting the edge of the CB, while non-metal doping changes the edge of the VB. In addition, the formation of a heterojunction not only adjusts the band gap energy, enhancing the light absorption capability, but also accelerates the transfer of electrons and/or holes, preventing the recombination of electron–hole pairs. According to different transfer pathways, as given in Fig. 1c, BiOX heterojunctions can be classified into Type I, Type II and Type Z.[11,12] From a Type I heterojunction, the electrons and holes transfer to the CB and VB of B from substance A, and the electrons in the CB and holes in the VB participate in the redox reaction. From a Type II heterojunction, the electrons transfer to the CB of B from substance A, and the holes transfer to the VB of A from B, and the electrons in the CB of B and holes in the VB of A participate in the redox reaction. From a Type Z heterojunction, the electrons transfer to the VB (hole) of A from substance B. The holes remained in B and the electrons in A participate in the redox reaction. Among the three heterojunctions, Z-scheme heterojunctions are regarded as one of the best ways to improve photocatalytic activity.[9] Besides the construction of heterojunctions, the decoration of BiOX by inorganic/organic frameworks, carbon materials, metal particles and carriers has been reported for enhancing the electronic conductivity, and promoting the transfer and separation rate of carriers, which restrains the recombination of electron–hole pairs.

Besides the design of photocatalysts, the selection of target organic pollutants also affects the photocatalytic activity. Up to now, various organic dyes are widely used, including Rhodamine B (Rh B), Methylene blue (MB), Methyl orange (MO), brilliant blue K-NR, and Alizarin Red S (ARS), *etc.* Besides organic dyes, all kinds of antibiotics have been selected as target pollutants, such as, ciprofloxacin (CIP), tetracycline (TC), tetracycline hydrochloride (TCH or TC-HCl), carbamazepine (CBZ), norfloxacin (NOR), atenolol (ATL), sulfamethoxazole (SMZ), levofloxacin (LVX), metronidazole (MTZ), ofloxacin (OFX), doxycycline (DOX), chlortetracycline hydrochloride, and so on. In addition, abundant organics can be degraded by BiOX-based photocatalysts, including phenol, bisphenol A (BPA), estriol, lindane, perfluorooctanoic acid (PFOA), 4-chlorophenol (4-CP), methanol, 4-dihydroxybenzoate (MDB), benzoic acid (BA), *p*-chloroaniline (PCA), diclofenac (DCF), benzyl alcohol, nitrobenzene, 17-ethinyl estradiol (EE2), 2,4-dihydroxybenzoate (MDB), and so on.

Herein, we introduce the recent progress on the different BiOX photocatalysts in degradation of organic pollutants. As shown in Fig. 2, synthetic methods decide the microstructure and the specific surface area of BiOX, which affect the photocatalytic activity. So the controllable synthesis of BiOX was introduced firstly, including hydrothermal or solvothermal method, hydrolysis, precipitation, two-phase method, ultrasonic/microwave assisted method, and physical method. Then, in the second part, the doping and surface modification

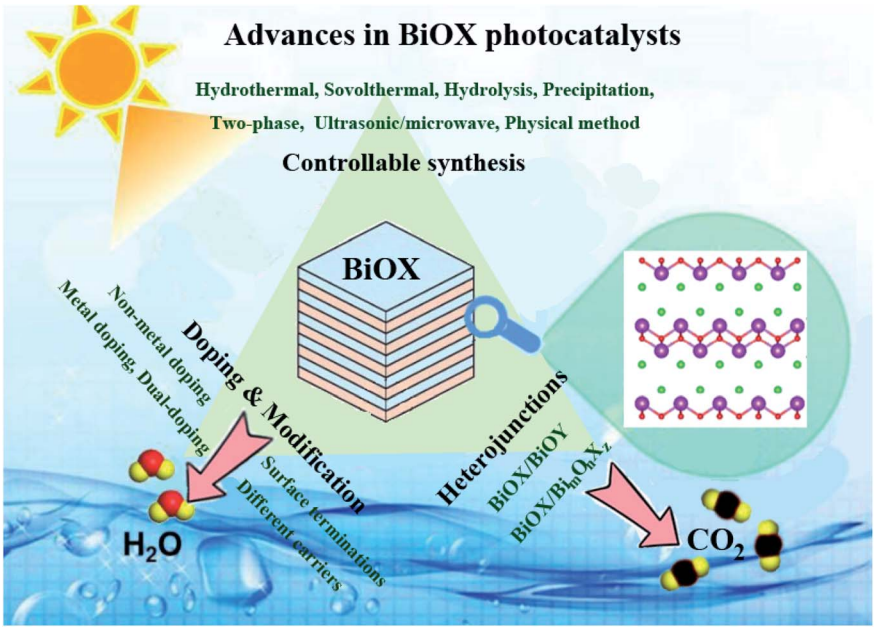

Fig. 2 Preparation and modification of BiOX photocatalysts for degradation of organic pollutants.

of BiOX was summarized. The heteroatom doping is devided into non-metal doping, metal doping and dual-doping. While in the respect of surface modification, different decoration terminations and carriers involved in modified BiOX were introduced. In the third part, the heterojunctions including BiOX/BiOY type and BiOX/$Bi_mO_nX_z$ system are summarized. At last, some promising research trends for developing high-performance BiOX photocatalyst are put forward. We expect that this review would provide practical guideline for the beginners in photocatalysis field.

2. Controllable synthesis of BiOX

The photocatalytic activity of BiOX photocatalysts mainly depends on their size, morphology, specific surface area and crystalline structure. Up to now, various BiOX species, including spheres, nanoflakes, sea urchins, flower spheres, hollow balls, and so on, have been synthesized for photocatalysts. In this section, we introduce the synthesis methods of different BiOX species, including hydrothermal, solvothermal, hydrolysis, precipitation method, two-phase method, ultrasonic/microwave-assisted method and physical method.

2.1. Hydrothermal method

In a typical hydrothermal process, the reactants including Bi source of $Bi(NO_3)_3 \cdot 5H_2O$ or $NaBiO_3 \cdot 2H_2O$, and the halogen source of NaX, KX, HX or ionic liquids are dissolved in water, and transferred into polytetrafluoroethylene (PTFE)-lined autoclave. Under a condition of high temperature and high pressure, various BiOX nanostructures were synthesized. During a reaction process, besides the precursors and their ratios, reaction temperature/time, the pH value of solution greatly affects the size and morphology of BiOX. In this field, Zhang *et al.*[13] confirmed that the BiOCl sheets prepared in alkaline solvent had the best photocatalytic oxidation performance on gaseous Hg^0 under UV light, due to the large specific surface area and a good growth orientation of crystal BiOCl. Similarly, BiOBr flakes were prepared *via* a hydrothermal method.[14] The sample prepared at the pH value of 9 displayed the highest degradation efficiency for removal of ciprofloxacin (CIP) under the irradiation of visible light. In addition, Intaphong *et al.*[15] found that pH value greatly affected the morphology, crystal structure of BiOBr and their photocatalytic performance. When the pH value was 8, the BiOBr microflowers were conducive to the uniform adsorption of Rh B molecules, which presented the best photodegradation performance for degradation of Rh B. Feng *et al.*[16] synthesized BiOBr by hydrothermal method, and changed the internal stress of BiOBr nanosheets through adjusting pH value. The low strain energy changed the symmetry and band structure of BiOBr, which enhanced the charge separation rate and the degradation rate of Rh B and MO dye.

During a hydrothermal process, various surfactants have been added to control the microstructure of BiOX. In this respect, Dou *et al.*[17] synthesized BiOI photocatalysts in glacial acetic acid by using $EO_{106}PO_{70}EO_{106}$ (F127) as a surfactant. A large specific surface area and much more hydroxyls on F127-BiOI accelerated the rapid separation of photogenerated carriers and promoted the formation of O_2^-. Zhou *et al.*[18] synthesized BiOCl nanosheets by using dulcitol ($C_6H_{14}O_6$) as surfactants. The thickness of BiOCl nanosheets were adjusted by changing the pH of solution. The BiOCl prepared at the pH value of 4 had a smaller thickness, which exhibited the best photocatalytic activity in the degradation of Rh B and TC-HCl, due to the best oxygen vacancy concentration and exposed (001) crystal plane. By using cationic polyacrylamide (C-PAM) as

a surfactant and chlorine source, Li *et al.*[19] synthesized tetragonal BiOCl nanosheets with exposed (001) facets. The BiOCl sample prepared at 150° for 12 h presented the highest degradation efficiency for the removal of MO. Through adjusting the amount of xylitol surfactants, Cai *et al.*[20] synthesized BiOCl nanosheets with different sizes. The sample prepared with 0.1 g xylitol showed a narrow band gap, a special polycrystalline structure, and a concentration of grain boundaries and oxygen vacancies, which degraded 98% Rh B in 20 min under visible light. Therefore, the selection of surfactants is crucial for enhancing the photocatalytic activity of BiOX.

2.2. Solvothermal method

Different from the aqueous solution in hydrothermal reaction, organic solvents are used in solvothermal reaction. Except for reaction conditions, the effect of solvent is indispensable. Various alcohols are adopted to synthesize BiOX. Among these alcohols, ethylene glycol is the commonly-used solvent.

By using EG-mediated solvothermal reaction, Gao *et al.*[21] prepared BiOCl microspheres for removal of carbamazepine (CBZ) under visible light. Tian *et al.*[22] synthesized core–shell hierarchical BiOCl microspheres. Rich oxygen vacancies formed on the BiOCl surface reduced the band gap and extended the light absorption range. The sample displayed the highest photocatalytic performance for degradation of norfloxacin (NOR) under visible light. By using EG as solvent, Mera *et al.*[23] synthesized BiOBr microspheres by using KBr precursor at 145° for 18 h, and the optimized sample degraded 97% MO in 60 min at the pH value of 2.

Mera *et al.*[24] synthesized two kinds of BiOI by using KI and 1-butyl-3-methylimidazolium iodide ([bmim]I) as iodine sources respectively. Through a comparison, the BiOI prepared with [bmim]I presented the best photocatalytic activity for removal of gallic acid, due to the highly exposed (001) facets. By using EG solvent, Jiang *et al.*[25] prepared hollow flower-shaped BiOI (h-BiOI). Compared to bulk BiOI, h-BiOI nanosheets with 2 nm thickness exhibited a larger specific surface area and stronger oxidation ability, which degraded 99% of Rh B within 60 min, much faster than that of bulk BiOI. Besides the single-phased BiOX, Zhang *et al.*[26] synthesized $BiOBr_xI_{1-x}$ nanoplates with exposed (001) crystal plane. Through decreasing the ratio of Br/I, the band gap reduced from 2.87 to 1.89 eV, which enhanced the light absorption. The optimized $BiOBr_{0.8}I_{0.2}$ showed the highest photocatalytic activity for degradation of Rh B, which was 5.4 and 1.7 times higher than that of BiOI and BiOBr, respectively.

During hydrothermal process, the type of solvent affects on the morphology, surface structure and performance of BiOCl. Zhao *et al.*[27] synthesized BiOCl with oxygen vacancies (OV-BOC) by using EG as solvent. Compared to pure BiOCl prepared with ethanol, the OV-BOC had a higher photocatalytic performance for degradation of Rh B, MO and phenol for the stronger oxidation capacity. In another work, ethanol, EG and glycerol was selected as solvents to synthesize BiOCl photocatalysts with different morphologies.[28] Through a comparison, BiOCl hierarchical microspheres prepared in EG solvent showed the highest photocatalytic activity for degradation of carbamazepine (CBZ), due to the enhanced adsorption capability and high separation efficiency. Xing *et al.*[29] synthesized different BiOBr photocatalysts by using water, ethanol, isobutanol, ethylene glycol, and glycerin. When used for photodegradation of reactive brilliant blue (KN-R), flower-like BiOBr prepared in glycerin presented the highest activity for the small size, exposed active face and abundant oxygen vacancies. Wei *et al.*[30] synthesized several BiOBr photocatalysts by using ethanol, ethylene glycol, *tert*-butanol, benzyl alcohol, and 2-methoxyethanol solvent. As a result, thin BiOBr nanosheets synthesized in benzyl alcohol presented the outstanding photocatalytic activity for degradation of Rh B, due to the exposed (001) facets. In addition, various BiOI photocatalyts were also synthesized by using water, ethanol, ethylene glycol and glycerin, respectively.[31] Among these samples, 3D mesoporous hierarchitectured BiOI prepared in glycerol displayed excellent visible-light photocatalytic activity for the removal of As(III), due to the largest specific surface area, mesoporous structure and highly exposed (001) facets. Dehghan *et al.*[32] prepared two kinds of BiOI photocatalysts by hydrolysis method and solvothermal method, and the sample prepared by solvothermal method showed an obvious superiority for degradation of tetracycline hydrochloride (TCH). Gao *et al.*[33] synthesized 3D mesoporous nanostructured BiOCl by adding PEG1000 into PEG400 solvent. Abundant mesopores and vacancies generated on thin BiOCl nanosheets (3–6 nm) effectively improved the photocatalytic activity for degradation of bisphenol A (BPA).

Besides the type of alcohols, the ratio of water/methanol also affects the morphology and performance of BiOCl. For example, Xu *et al.*[34] synthesized BiOCl nanosheets with different sizes and shapes through adjusting the water/methanol ratios. When the water content was 10%, the prepared BiOCl exhibited a small size and thickness, with largely exposed {001} facets, which presented superior photocatalytic activity for degradation of MO and Rh B. In addition, Lee *et al.*[35] synthesized BiOX (X: Cl, Br, I) microspheres by using ethanol/EG mixture solvent. When used for photocatalytic hydrogen evolution, flower-like BiOI microspheres exhibited the highest photocatalytic activity for the lower fluorescence intensity.

2.3. Hydrolysis method

In a typical hydrolysis process, $Bi(NO_3)_3 \cdot 5H_2O$, $BiBr_3$ or $NaBiO_3 \cdot 2H_2O$ is often used as Bi sources. After the solution of halide sources was dropped to the solution of Bi source, the BiOX can be produced under the mechanical stirring. The precursor types and their concentrations have a great influence on the morphology and performance of BiOX. Moreover, solvent affects the growth of BiOX crystals, which also decides the photocatalytic performance. By using a hydrolysis method, Hu *et al.*[36] synthesized BiOCl photocatalyst for degradation of atenolol (ATL), and the removal efficiency reached nearly 100% within 60 min. Song *et al.*[37] synthesized BiOCl nanosheets for degradation of perfluorooctanoic acid (PFOA). Under the irradiation of UV light, the BiOCl decomposed nearly 100% PFOA within 12 h, and the degradation rate constant was 14.6 and 1.7

times higher than that of commercial TiO_2 (P25) and In_2O_3. Zhang *et al.*[38] synthesized thin BiOCl nanosheets with a thickness of 20 nm. When used for degradation of Rh B, the BiOCl exhibited a higher photocatalytic activity than degradation of MO and MB. Yuan *et al.*[39] synthesized ultrathin BiOBr nanoflakes, and the ultrathin nanocrystals exhibited a higher photocatalytic activity for degradation of Rh B under visible light, much better than that of 3D BiOBr microspheres and P25-TiO_2. By using $BiBr_3$ as precursor, Li *et al.*[40] synthesized nanosheet, honeycomb, and flower-like BiOBr photocatalysts by using water, ethanol (EtOH) and isopropyl alcohol (IPA), respectively. Through a comparison, the BiOBr nanosheets prepared in water presented the best crystallinity and superior photocatalytic activity for degradation of MO. By controlling the amount of water, Lu *et al.*[41] prepared BiOI with surface heterojunction between (001) facets and (110) facets. The interface junction in BiOI promoted the separation of electron–hole pairs, and enhanced the photocatalytic activity for degradation of MO. In addition, Ahern *et al.*[42] synthesized BiOCl and BiOI *via* a hydrolysis method for degradation of 17-ethinyl estradiol (EE2) and estriol in water. Through a comparison, BiOI displayed the highest activity under 350 nm light source, while the BiOCl had the highest activity under 254 nm light source.

2.4. Precipitation method

In a typical precipitation method, alkali solution containing halide sources was slowly dropped into the Bi-containing precursors. Under the stirring, BiOX were precipitated. Followed by this method, Zhang *et al.*[43] synthesized BiOCl, BiOBr and BiOI photocatalysts respectively. When used for the removal of Hg^0 under the irradiation of fluorescent light, the activity sequence was BiOI > BiOBr > BiOCl, and BiOI exhibited the best photocatalytic performance. Huang *et al.*[44] synthesized Br^- substituted BiOI (Br-BiOI) photocatalyst by introduction of Br^- into BiOI lattice. The replacement by Br^- reduced the valence band potential and enlarged band gap, which suppressed the recombination of electron–hole pairs and enhanced the photocatalytic activity of BiOI. In addition, the photocatalytic activity of BiOX can be improved by adjusting the band engineering. In this respect, $Bi_{24}O_{31}Cl_{10}$ powders were synthesized *via* a chemical precipitation method.[45] The $Bi_{24}O_{31}Cl_{10}$ had a narrow band gap, which presented a superior photocatalytic activity for degradation of Rh B under visible light.

2.5. Two-phase method

Besides traditional synthetic methods, two-phase reaction was used to synthesize BiOCl nanosheet at the water–air interface.[46] The resulting BiOCl nanosheets with exposed (010) facets presented a high photocatalytic activity for degradation of methyl orange (MO). In another two-phase method,[47] octadecene (ODE), oleic acid (OA) and oleylamine (OLA) was acted as oil phase to dissolve $Bi(NO_3)_3 \cdot 5H_2O$, and the aqueous solution of KX (X = Cl, Br, I) was acted as water phase. After the mixed solution was refluxed at 170 °C, ultrathin 2D BiOX nanosheets were synthesized. During the preparation process, acidic condition enabled the formation of ultrathin BiOX structure with highly exposed {001} facets.

2.6. Ultrasonic/microwave-assisted method

Based on traditional chemical bath method, Intaphong *et al.*[48] synthesized BiOI nanoplates *via* a sonochemical method in ultrasonic bath at 80 °C, and the BiOI nanoplates prepared in the pH of 12 exhibited the highest efficiency for degradation of Rh B under visible light. Furthermore, microwave-assisted method was used to synthesize BiOI and BiOBr in a short time. Montoya-Zamora *et al.*[49] synthesized BiOI photocatalyst *via* microwave-assisted method with EDTA retarder. The sample prepared with 40% of EDTA at 110 °C had the highest specific surface area, which presented the highest photocatalytic activity in degradation of Rh B. In addition, Miao *et al.*[50] synthesized BiOBr hierarchical microcubes *via* microwave-assisted ionothermal self-assembly method. Multi-layered BiOBr nanosheets were formed and exhibited a strong light harvesting ability. Chen *et al.*[51] synthesized porous and hollow BiOBr microspheres *via* a microwave-assisted solvothermal route within 20 min. Compared to the hollow microspheres, porous BiOBr spheres showed a higher photocatalytic activity for degradation of Rh B, due to the large surface area, small particle size and narrow band gap.

2.7. Physical methods

Some physical methods, including combustion or calcinations, ultrasonic exfoliation, and mechanical grinding have been reported for synthesizing BiOX photocatalysts. A simple one-step combustion method was developed to synthesize BiOBr nanosheets with exposed {001} facets.[52] The proportion of exposed {001} facets could be adjusted by changing the amount of ammonium bromide, which further narrowed the band gap energy of BiOBr. The BiOBr-5 sample with a thickness of 193 nm presented the highest photocatalytic activity for degradation of Rh B under visible light. In addition, electrospinning method[53] was adopted to generate nanofibers containing $BiBr_3$ precursors firstly, and the post calcination was conducted at 500 °C in air to prepare BiOBr with lamellae nanostructures. Through adjusting $BiBr_3$ content in PAN solution, the optimized BiOBr with 3% $BiBr_3$ displayed the best performance for degradation of Alizarin Red S (ARS).

Ultrasonic exfoliation method[54] was developed to fabricate monolayered BiOBr nanosheets with a thickness of ~0.85 nm in formamide solvent. The monolayered BiOBr exhibited a higher adsorption and photodegradation performance. A simple solvent-free mechanical grinding method was developed for preparing BiOCl, BiOBr, and BiOI hierarchical flower-like nanostructures with a thickness of 5 min.[55] Three BiOX samples possessed excellent photocatalytic activities for photodecomposition of MB and Rh B. Due to the short preparation time and excellent photocatalytic activity, the solvent-free grinding strategy can be adopted for achieving the mass production of BiOX.

2.8. Summary

Synthetic method decides the microstructure and performance of BiOX photocatalysts. In this section, we introduce the controllable synthesis of BiOX photocatalysts. In order to make a comparsion, synthesis method, morphology and photocatalytic performance of BiOCl, BiOBr and BiOI are listed in Table S1.† Among these methods, hydrothermal and solvothermal method are the most popular route for synthesizing BiOX. Compared to hydrothermal method, the selection of solvents is really important in solvothermal reaction. Various alcohols, including methanol, ethanol, ethylene glycol, *tert*-butanol, benzyl alcohol, and PEG-400 have been used as solvents for synthesizing BiOX. Through a comparison, the BiOX prepared with EG usually exhibits a superior photocatalytic activity than the sample prepared by monohydric alcohols. Besides the influence of the reaction temperature/time, surfactants and halide precursors are also essential for the morphology and performance of BiOX. Halide-containing ionic liquids are often used for fabricating hierarchical spherical BiOX with a high photocatalytic activity. However, these ionic liquids are much more expensive than traditional halide source KX or NaX, further limiting their wide application. Two-phase method and precipitation method can be adopted to prepare BiOX nanosheets with highly exposed (010) facets, while these methods are seldom accepted by researchers. Based on solution-based reaction, microwave-assisted strategy greatly shortens the reaction time, and improves the production efficiency. Different from solution-based synthetic methods, some physical methods including calcinations and mechanical grinding method, exhibit a promising application potential for the mass production of BiOX photocatalysts.

3. The doping and surface modification of BiOX

Except for the microstructure control of BiOX, the heteroatom doping and surface modification can be adopted for improving the photocatalytic activity of BiOX. The heteroatom doping is introducing nonmetal or metal heteroatoms to the crystal plane, further reducing the band gap, extending the light absorbance range and promoting the separation of photogenerated carriers.[56] According to the species of doped element, we classify the doping into non-metal doping, metal doping and dual doping, and recent advance of doped BiOX photocatalysts was summarized. Different from the heteroatom doping, surface modification of BiOX has a wide research range. On the one hand, surface defects or surface terminations can be introduced on the surface of BiOX. On the other hand, various decorators including inorganic/organic frameworks, carbon materials, metal particles, and carriers can be used to hybridize with BiOX. After the surface modification, the electronic conductivity and the light absorption capability of BiOX will be improved, which further accelerate the transfer and separation of charge carriers, and effectively inhibit the recombination of electron–hole pairs.

3.1. The doping of BiOX

3.1.1 Non-metal doping. Among non-metal elements, boron (B), carbon (C), nitrogen (N), sulfur (S) and iodine(I) have been reported as dopants for preparing non-metal doped BiOCl, BiOBr, and BiOI. Among these non-metal elements, B has a small ion radius of about 0.023 nm. The light weight and semiconductivity facilitate the diffusion of B in BiOX crystal structure. In this field, Yu *et al.*[57] prepared B-doped BiOCl (B-BiOCl) photocatalysts with borax as boron source *via* a solvothermal method. B-doping increased the specific surface area. Moreover, the exposed (001) facets in B-BiOCl nanosheets enhanced the separation efficiency of charges. Therefore, the optimized $B_{1.0}$-BiOCl showed a high photocatalytic activity for degradation of bisphenol A, phenol and Rh B, much better than pure BiOCl. Liu *et al.*[58] synthesized B-doped BiOBr photocatalysts with hierarchical microspheres for degradation of Rh B and phenol. The B dopants were introduced into BiOBr lattice in substitutional mode, and the B-doped BiOBr exhibited hydroxyl groups-enriched surfaces, which promoted the adsorption of dye molecules and the separation efficiency of photogenerated carriers. Except for the experimental research, first-principles calculation has been reported to observe the B-doping and P-doping in single-layer BiOBr.[59] The P-doping effectively reduced the band gap of BiOBr, while B-doping extended the visible light absorption range and reduced the recombination rate of photogenerated carriers. The calculation results showed that B-doping increased catalytic active sites. Therefore, B-doped BiOBr was confirmed as a practical strategy for enhancing the photodegradation performance.

In addition, C doping also accelerates the transfer and separation of photo-generated charges separation. In this respect, Zeng *et al.*[60] synthesized C-doped BiOI (C-BiOI) photocatalysts by using glucose as carbon sources, as shown in Fig. 3a. Doped carbon clusters embedded into the interlayers of BiOI structure increased the specific surface area, adjusted the lattice periodicity, and produced vacancies, which reduced the band gap and enhanced charge separation efficiency. When used for degradation of methyl orange (MO), the degradation rate of optimized C-BiOI was 4.44 times higher than that of pure BiOI. Qu *et al.*[61] synthesized graphene oxide (GO) and carbon nanodots (CDots) co-doped BiOBr (GO/CDots/BiOBr) composites. In this ternary composite, GO was acting as the electron-transfer and electron-reservoir center and suppressed the recombination of electron–hole pairs. The CDots enhanced the visible light harvesting and utilizing ability of BiOBr. So the GO/CDots/BiOBr exhibited the highest photocatalytic activity for degradation of 4-chlorophenol (4-CP) under visible light. In addition, N-doped BiOBr nanosheets were decorated on the surface of carbon fibers (CFs) through a solvothermal method.[62] Due to the strong visible-light absorption from all directions, 3D N-doped BiOBr/CFs exhibited an outstanding photocatalytic activity for degradation of Rh B and methanol.

S-doped BiOCl and BiOBr have been reported in recent years. For instance, Shang *et al.*[63] synthesized S-doped BiOCl (BiOCl-S, Fig. 3b) by using thioacetamide as sulfur source. The crystal structure of S-doped BiOCl had no change. While S doping

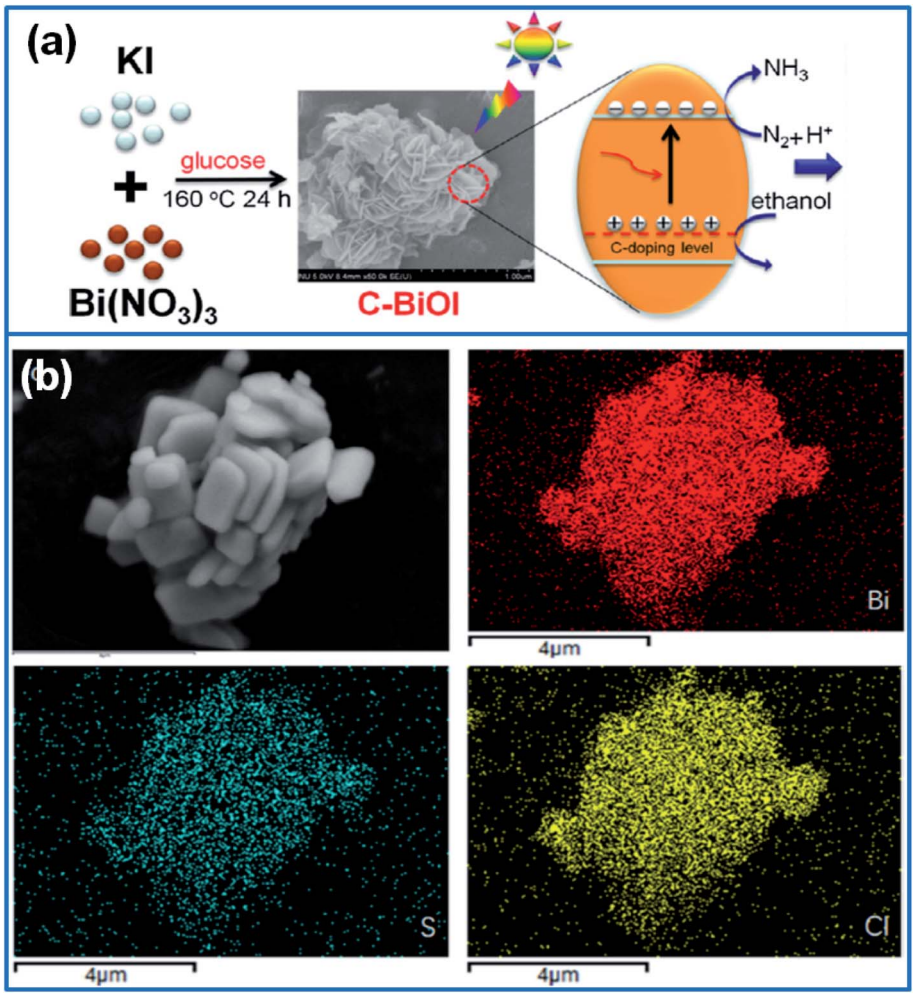

Fig. 3 (a) Preparation of C-BiOI photocatalysts by using glucose as carbon sources for degradation of organic pollutants.[60] Copyright 2019 Elsevier. (b) The microstructure of BiOCl-S and its element mapping.[63] Copyright 2018 Elsevier.

broadened the light absorption edge, which enhanced the visible light absorption ability. Moreover, S doping suppressed the recombination of electron–hole pairs of BiOCl. So the BiOCl-S exhibited a superior photocatalytic activity for degradation of Rh B and phenol. Jiang *et al.*[64] prepared BiOCl-S photocatalysts *via* a solvothermal method. The uniform dispersion of S elements on BiOCl extended the light absorption range and promoted the separation of electron–hole pairs. In addition, S-doping can be adopted to tailor the band structure of BiOBr. In this field, Wang *et al.*[65] synthesized S-doped BiOBr with a thickness of ~10 nm *via* hydrothermal method. S doping narrowed the band gap of BiOBr, and enabled the BiOBr with a strong visible-light response. Furthermore, S doping improved the charge separation efficiency. As a result, optimized $S_{0.2}$-BiOBr nanosheets presented the highest activity for degradation of bisphenol A (BPA) under visible light irradiation. Zhang *et al.*[66] prepared I-doped BiOCl microspheres by a microwave-assisted method. I doping increased the specific surface area of BiOCl, narrowed the band gap, and promoted the separation of photogenerated carriers. Therefore, I-doped BiOCl achieved a high removal ratio of 91.2% in 60 min for degradation of 2,4-dihydroxybenzoate (MDB).

3.1.2 Metal doping. Besides non-metal doping, various metals including Al, Zn, Sn, In and Pt have been reported for preparing metal doped BiOX. In this respect, Zhang *et al.*[67] synthesized Al-doped BiOCl microspheres *via* a solvothermal method. Al doping increased the specific surface area, enabled the BiOCl with sunlight absorption capability and fast charge separation. The optimized Al-10.0-BiOCl with Al/Bi ratio of 1/10 degraded 91.1% TCH in 60 min under simulated sunlight. Li *et al.*[68] synthesized Zn-doped BiOCl hierarchical nanostructures *via* ethylene glycol (EG)-assisted solvothermal route. Zn doping only affected the photocurrent and BET surface area, without changing the particle size and morphology. Optimized Zn-doped BiOCl fastly degraded almost all Rh B in 8 min. However, Zn-doped BiOBr photocatalyst had been confirmed a poor photocatalytic activity,[69] due to the weak visible light absorption.

Sn-doped BiOCl was synthesized with a tetragonal crystal structure by using $SnCl_2$ as reactant *via* an oxidation–reduction method.[70] After doping with Sn, the surface of BiOCl was

rougher, and the band gap energy was narrowed. Tetra-valence Sn (10%) doped BiOCl enhanced the photocatalytic activity for degradation of Rh B and benzoic acid (BA). Li *et al.*[71] synthesized In-doped BiOI (In-BiOI) photocatalysts with exposed {001} facets *via* co-precipitation and hydrothermal method. In-doping did not change the specific surface area, microstructure or light absorption range, only improved the charge separation efficiency. The optimized In-BiOI exhibited an enhanced photocatalytic activity for degradation of *p*-chloroaniline (PCA) and MO under visible light. In addition, noble metal ion Pt^{4+} was filled into Bi defects on the BiOCl surface to adjust the surface atoms.[72] Pt^{4+} doping enhanced the light absorption and separation efficiency of electron–hole pairs, so PtO/Pt^{4+}-BiOCl photocatalyst exhibited an excellent degradation performance for removal of sulfamethoxazole (SMZ).

Among the transition metals, Co, Fe, Ti, Mn, W, and Nb have been used for preparing doped BiOX. For example, Wang *et al.*[73] synthesized Co-doped BiOCl nanosheets *via* hydrothermal method. The Co-doping accelerated the charge transfer by producing a doping energy level in the band gap of BiOCl. Moreover, Co-doped BiOCl exhibited a strong visible light response through extending the light absorption range. When used for degradation of BPA under visible light, Co-doped BiOCl nanosheets presented 3.5 times higher degradation rate than that of BiOCl.

In addition, Fe-doped BiOCl nanosheets were synthesized for degradation of levofloxacin (LVX) under LED light irradiation.[74] As shown in Fig. 4a, Fe-doping adjusted the energy band structure, expanded visible light absorption range, and promoted the charge separation. As a result, Fe-doped BiOCl achieved the fast degradation of 95% LVX in 60 min, with a superior reusability for five cycles. Liu *et al.*[75] synthesized Ti-doped BiOI microspheres (Fig. 4b) for degradation of diclofenac (DCF) under visible light. The Ti doping broadened the energy gap through producing more negative conduction band edge, which induced the generation of more $^{\bullet}O_2^-$ radicals during photocatalysis process. The optimized sample removed 99.2% of DCF within 90 min, and the kinetics constant was ~12 times higher than that of pure BiOI.

Manganese (Mn) can be used as a suitable dopant for BiOCl, due to multiple valence states and low cost. The experiment results confirmed that Mn-doping promoted the separation of photoinduced carriers, and enhanced the light absorption region through forming an intermediate energy level. Moreover, Mn cations in doped BiOCl generated abundant active oxygen species.[76] Therefore, Mn-doped BiOCl photocatalysts have been reported for degrading 94.3% metronidazole (MTZ) in 15 min under simulated sunlight, degrading 98% malachite green in 120 min under visible light,[77] and removing 58.8% Rh B in 120 min under UV irradiation.[78] Therefore, Mn-BiOCl can be used to treat various wastewaters containing antibiotics or organic dyes. Mokhtari *et al.*[79] synthesized W-doped BiOCl nanosheets through a hydrothermal method. W-doped BiOCl exhibited a high photocatalytic activity for degradation of Rh B under both visible light and UV irradiation, due to the reduced band gap and expanded light absorption region. In addition, niobium-doped BiOBr (Nb-BiOBr, Fig. 4b) were prepared for degradation of Rh B and ofloxacin (OFX) under visible light.[80] Nb-doping increased the specific surface area, extended the light absorption range, and promoted the separation of photogenerated carriers. The optimized 1.25Nb-BiOBr sample showed the highest photocatalytic activity in degradation of Rh B and OFX. Yu *et al.*[81] synthesized Bi-modified Nb-doped oxygen defective BiOCl microflowers *via* solvothermal method. The deposited Bi on BiOCl surface acted as the medium for transferring electrons, while the doping of Nb^{5+} was served as electron traps by adjusting the energy level of the CB of BiOCl. The doping of Nb^{5+} and modification by Bi^0 expanded the visible light absorption, promoted the transfer of electrons and the separation of electron–hole pairs. Therefore, the modified BiOCl with the Nb/Bi of 1/7 delivered a superior photocatalytic activity for degradation of Rh B and Tetracycline (TC) under visible light, and the kinetics constant increased by 134% (Rh B) and 82% (TC), respectively.

In view of the up-conversion luminescence induced by lanthanides ions (Ln-ions),[82] lanthanide metals including La, Ce, Y, Yb, and Er, have been used to dope BiOX by combining the photocatalysis with luminescent emission. In this field, Xu *et al.*[83] prepared La-doped BiOCl nano-/micro-structures with ginkgo-leaf-like "petals" based on Ostwald ripening mechanism. The La-doped BiOCl film showed narrow band gap energy, which delivered a superior photocatalytic activity for degradation of Rh B under simulated sunlight. In another work, La^{3+}-doped BiOBr microspheres were fabricated by using 1-hexadecyl-3-methylimidazolium bromide ([C16mim]Br)-assisted solvothermal method.[84] La^{3+} doping reduced the band gap and promoted the fast separation of electron–hole pairs, which presented an enhanced photocatalytic activity for degradation of Rh B and ciprofloxacin (CIP).

In addition, Ce-doped BiOBr nanoplates were prepared *via* hydrothermal method for degrading Rh B under visible light.[85] Ce^{3+} ions were embedded into BiOBr crystal lattice, which increased the specific surface area, induced the blue shift of the adsorption edge and broadened the band gap of BiOBr. Ce-doped BiOBr achieved the fast degradation of 99.22% Rh B in 40 min, and the kinetic constant was 3 times higher than that of pure BiOBr. Zhong *et al.*[86] synthesized yttrium-doped BiOCl (Y-BiOCl) for removal of tetracycline hydrochloride (TC). The doped Y^{3+} displaced Bi^{3+} ions in BiOCl lattices and caused the lattice distortion, which increased the concentration of oxygen defects and holes. Furthermore, Y^{3+}-doping reduced the bandgap energy of BiOCl, and suppressed the recombination of photocarriers. As a result, 15 wt% Y-doped BiOCl degraded 90.3% TC within 60 min under visible light irradiation. Ytterbium ions (Yb^{3+}) doped BiOI 3D nanoflowers were also synthesized *via* solvothermal method.[87] Yb^{3+} ions doping enabled the BiOI with a capacity to up-convert near-IR light into visible light, and enhanced the separation efficiency of electron–hole pairs. The degradation efficiency of 2%-Yb: BiOI was two times higher than that of pure BiOI for degrading Rh B. Moreover, Yb^{3+}-doped BiOI also showed a high activity for photodegradation of herbicide isoproturon. Peng *et al.*[88] prepared Er^{3+} doped BiOI nanosheets by using water and ethylene glycol as mixed solvent *via* microwave-assisted

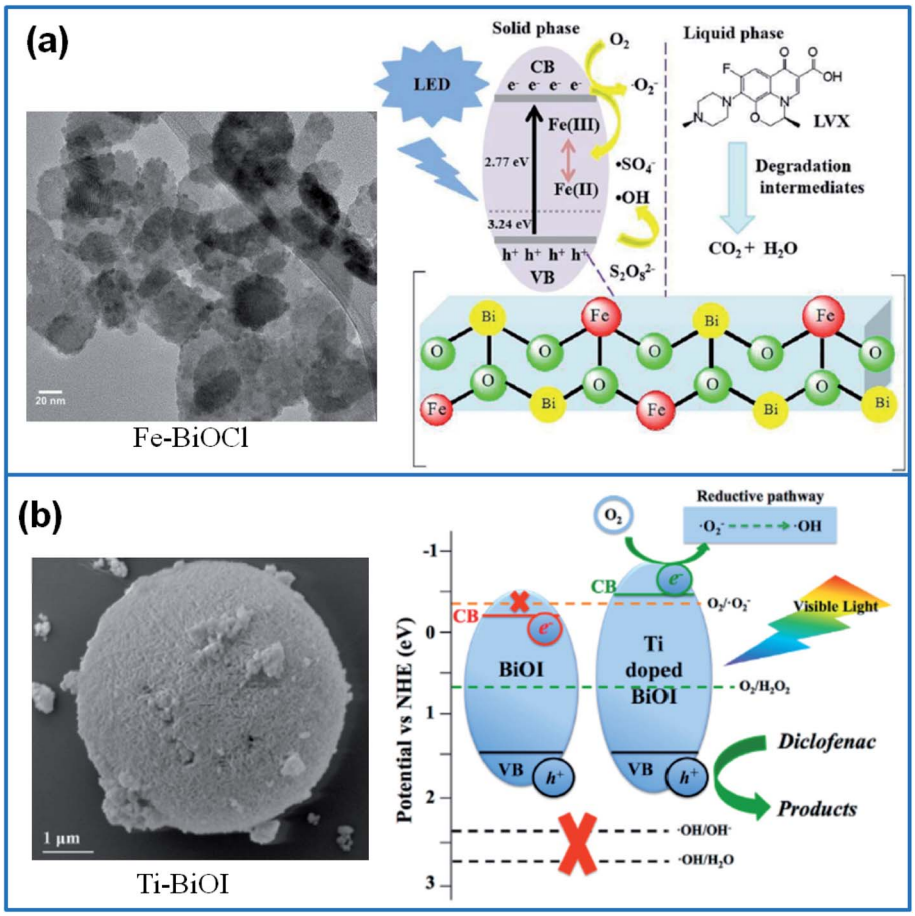

Fig. 4 (a) TEM image of Fe-BiOCl nanosheets and their photocatalytic mechanism.[74] Copyright 2020 Elsevier. (b) SEM image of Ti doped BiOI and the photocatalytic mechanism.[75] Copyright 2019 Elsevier.

solvothermal route. The doping of Er^{3+} ions decreased the energy level of BiOI conduction band, which enhanced the electron capture capability of BiOI, and prevented the recombination of the electron–hole pairs. Therefore, Er^{3+} doped BiOI nanosheets presented an excellent photocatalytic activity for degradation of Rh B and MO under visible light.

3.1.3 Dual doping of BiOX. To further enhance the photocatalytic performance of BiOX, dual doping by non-metal and metal or two metals has been reported. In this field, He *et al.*[89] prepared Bi quantum dots (QDs) implanted C-doped BiOCl (C/BOC/B) photocatalysts *via* solvothermal method. When used for NO_x removal, the Bi QDs acted as electron-donating and light-capture sites, and doped C atoms induced the charge transfer from Bi QDs to BiOCl. Due to the synergistic effect of Bi QDs and doped C heteroatoms, the C/BOC/B photocatalyst showed a superior photocatalytic activity for NO conversion. In another work, single atom-dispersed Ag and carbon dots (CDots) co-doped BiOI microspheres (Ag/CDots/BiOI) were synthesized by using 1-butyl-3-methylimidazolium iodine ([Bmim]I) ionic liquids.[90] The interaction between CDots and Ag broadened the visible light absorption of BiOI and improved the photocatalytic activity. Furthermore, CDots produced up-converted PL properties, metallic Ag had a SPR effect, and the composite facilitated the electron transfer from BiOI to Ag, then to CDots, thus promoting the separation of carriers. As a result, the 0.9-Ag/2-CDots/BiOI sample with 0.9 wt% of Ag and 2 wt% of CDots exhibited the highest photocatalytic activity for removal of 4-chlorophenol (4-CP) under visible light. In addition, Fe and N co-doped BiOBr photocatalysts (Fe-BiOBr-N) with flower-like structures were fabricated *via* a microwave-assisted solvothermal route.[91] Fe, N co-doping reduced the band gap to 1.92 eV from 2.87, increased the surface area, and inhibited the recombination of photogenerated carriers. When used for removal of bisphenol A (BPA), Fe-BiOBr-N presented a superior photocatalytic activity under visible light, much better than BiOBr-N, Fe-BiOBr and pure BiOBr.

In the field of two metals doping, Nussbaum *et al.*[92] synthesized Fe, Nb co-doped BiOCl by a co-precipitation method. The Fe, Nb co-doped BiOCl generated a strong interaction between the adsorbent and adsorbate (dye molecules), which contributed to the enhanced photocatalytic activity for degradation of Rh B. Yu *et al.*[93] synthesized Er^{3+} and/or Yb^{3+} ions doped BiOCl *via* hydrothermal route. With an increase of the Ln doping amount, the thickness of BiOCl sheets decreased to ~80 nm from ~140 nm. The BiOCl sheets doped with 2.0% Yb^{3+} and 0.5% Er^{3+} showed the highest photocatalytic activity

under visible light, which degraded 99.5% Rh B in 20 min. The degradation efficiency was 2.8 times higher than that of pure BiOCl. Niu *et al.*[94] synthesized 3D flower-like Ho^{3+}/Yb^{3+} and Er^{3+}/Yb^{3+} co-doped BiOCl photocatalysts *via* a hydrothermal route respectively. The doping by 0.5% Ho^{3+}/10% Yb^{3+} and 0.5% Er^{3+}/10% Yb^{3+} ion pairs reduced the band gap to 2.65 and 2.58 eV from original 3.1 eV of pure BiOCl, which effectively suppressed the recombination of electron–hole pairs. Furthermore, co-doping extended the UV absorption to near infrared light and blue light. Therefore, Ho^{3+}/Yb^{3+} and Er^{3+}/Yb^{3+} co-doped BiOCl exhibited a superior photocatalytic performance for removal of Rh B under simulated sunlight and 450 nm blue light.

3.2. Surface modification

Surface modification of BiOX involves a wide research range. For example, we can introduce surface defects or surface terminations on the surface of BiOX. Furthermore, inorganic/organic frameworks, carbon materials, metal particles, and different carriers can be adopted to modify BiOX.

3.2.1 Surface engineering. Modification of surface atomic structures, especially surface terminations could create oxygen vacancies or defects, which greatly affects the photocatalytic performance of BiOX. Some alcohols including methanol (METH), ethanol (ETH), *n*-propyl alcohol (NPA), propylene glycol (PG), or glycerol (GLY) can be used to tailor the surface structure of BiOX. Surface hydroxyls not only enhance the photooxidative ability, but also promote the photocatalytic reaction. In this field, Wu *et al.* prepared defective BiOCl through the surface reorganizations *via* ethylene glycol treatment.[95] The surface reorganization improved the photocatalytic activity of BiOCl by increasing the mobility of carriers and expanding visible-light absorption edge. Wei *et al.*[96] modified hierarchical BiOBr microspheres by using different imidazole ionic liquids. The resulting BiOBr-C4-Br, BiOBr-BF4 and BiOBr-PF6 were corresponding to the sample modified by 1-butyl-3-methylimidazolium bromide, 1-butyl-3-methylimidazolium tetra-fluoroborate and 1-butyl-3-methyl- imidazole hexa-fluorophosphate, respectively. Various ionic liquids induced the variation of oxygen vacancies and crystal surfaces, which greatly affected the separation efficiency of photoelectron–hole pairs. Through a comparison, BiOBr-C4-Br presented the highest photocatalytic activity for degradation of MO and tetracycline hydrochloride, due to the lowest proportion of (011) facets. Therefore, surface modification of BiOX is a practical strategy for enhancing the photocatalytic activity of BiOX.

3.2.2 Decoration with inorganic/organic frameworks. As nitrogen-rich organic porous materials, covalent triazine frameworks (CTFs) have π-stacked aromatic units, which can be used to degrade organic pollutants through accelerating the photogenerated electron separation and charge transfer. In this field, BiOBr/CTF-3D composite was synthesized for degradation of TCH and CIP under visible light.[97] The BiOBr/CTF-3D composite containing 2 wt% CTF-3D presented the highest photocatalytic activity, due to the enhanced light adsorption range, and the high separation efficiency of photogenerated electron–hole pairs. Similar to the CTFs, metal–organic frameworks (MOFs) have a regular pore structure and superior adsorption ability. Various MOFs were used to hybridize with BiOX.[98,99] In this field, Jiang *et al.*[100] prepared titanium dicarboxylate MIL-125(Ti) modified BiOI composites (BiOI/MIL-125(Ti)) *via* hydrothermal method. BiOI was uniformly generated on MIL-125(Ti) surface to form heterostructure, which also increased the specific surface area, promoted the charge transfer, and extended the visible light absorption.

3.2.3 Decoration with carbon materials. Among the carbon materials, carbon nanotubes (CNTs), C70 and carbon quantum dots can be acted as an electron-acceptor/transport matrix in photocatalysis for the excellent electronic properties.[101] In this respect, Li *et al.*[102] synthesized multiwalled carbon nanotubes (MWCNTs) decorated BiOI nanosheets *via* a solvothermal method (Fig. 5a). The coupling interface between BiOI and MWCNTs promoted the separation of electron–hole pairs, and facilitated the absorption of visible light. The composite with 3 wt% MWCNTs presented the highest activity for degradation of Rh B, MO, and *para*-chlorophenol (4-CP) under visible light. Similar to CNTs, C70 has excellent electron acceptability for the delocalized conjugated structure.[103] Ma *et al.*[104] prepared unique flower-like C70 modified BiOBr photocatalysts *via* hydrothermal method. The decoration of C70 introduced more hydroxyl groups on sample surface. Moreover, it also promoted the separation of photoexcited carriers. The C70/BiOBr exhibited an outstanding photocatalytic activity for degradation of phenol and Rh B under simulated sunlight. In addition, carbon quantum dots (CQDs) modified BiOBr or BiOCl nanosheets were synthesized *via* an ionic liquid induced method.[105] As shown in Fig. 5b, CQDs uniformly dispersed on BiOX nanosheets reduced the resistance, enhanced the visible light absorbance and the separation efficiency of electrons and holes. The CQDs/BiOBr nanosheets containing 3 wt% CQDs delivered the maximum photocatalytic activity for degradation of Rh B, CIP and bisphenol A.

3.2.4 Decoration with metal particles. Metal Bi has been demonstrated as a co-catalyst to improve the photocatalytic properties of semiconductors through playing direct plasmonic photocatalytic performance.[106] Recently, various Bi/BiOCl heterostructures have been reported for enhancing the photocatalytic activity of BiOCl.[107] For instance, Bi nanowires@BiOCl nanosheets composites[108] and Bi decorated defective BiOCl hierarchical microspheres[109] were fabricated, and the enhanced photocatalytic activity was ascribed to the synergistic role of Bi metal and oxygen vacancies in BiOCl. In addition, Bi nanoparticles decorated BiOBr composites (Bi/BiOBr) were prepared by using glycerol solvent.[110] The deposited Bi particles produced abundant oxygen vacancies, and formed Bi/BiOBr heterostructure, which promoted the separation of photoinduced electron–hole pairs by acting as the electron traps. As a result, Bi-decorated BiOBr presented a high photocatalytic activity for degradation of phenol. In another work, Bi/BiOBr hollow microspheres with oxygen vacancies were synthesized *via* solvothermal method.[111] The hollow structure increased the specific surface area, which enhanced the adsorption ability. Moreover, abundant oxygen vacancies improved the light

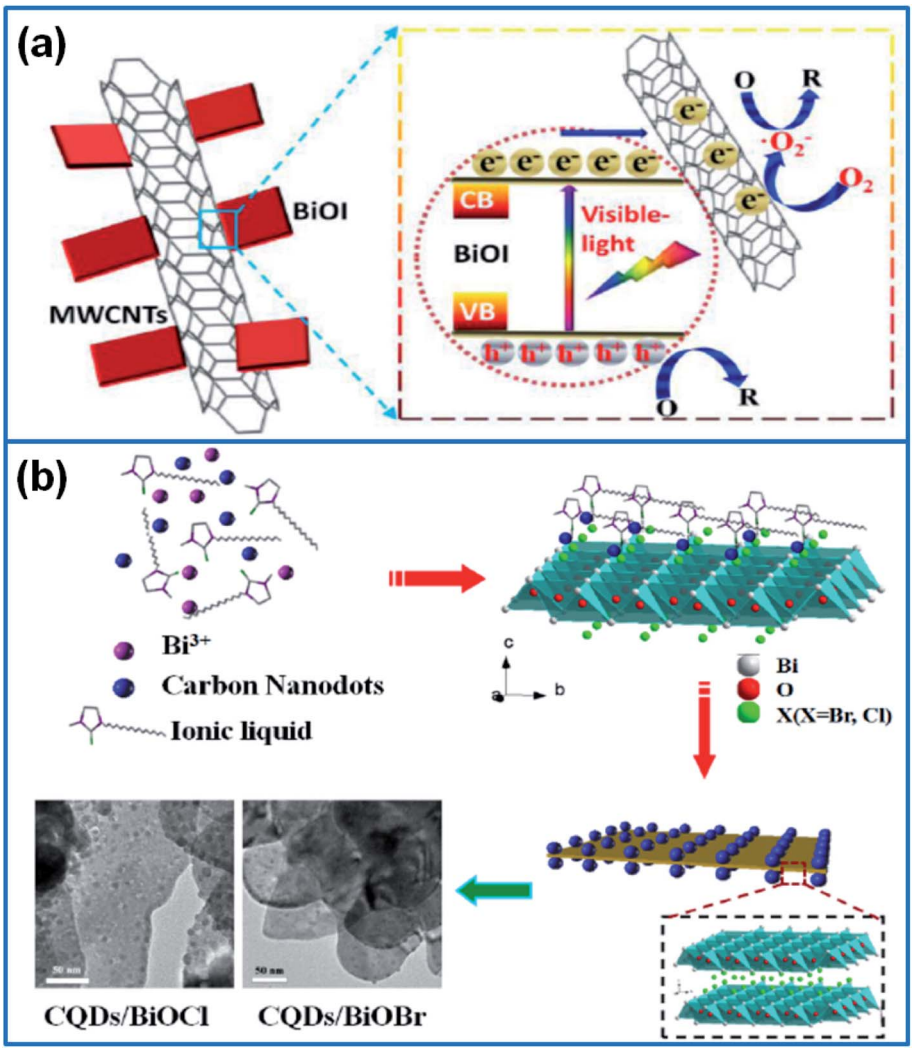

Fig. 5 (a) Photocatalytic mechanism of MWCNTs/BiOI photocatalyst.[102] (b) Schematic illustration of the preparation of CQDs/BiOX hybrid nanosheets and the microstructure by TEM.[105] Copyright 2016 Elsevier.

absorption ability. Therefore, the optimized Bi/BiOBr presented a higher photocatalytic activity for degradation of Rh B than pure BiOBr. Cao *et al.*[112] synthesized hierarchical microflower-like Bi/BiOBr heterostructure *via* a solvothermal route. Bi nanoparticles decorated on BiOBr surface suppressed the agglomeration of nanoparticles and introduced more active sites, which facilitated the separation of electron–hole pairs. The Bi/BiOBr photocatalyst achieved the complete degradation of the coexisting system of TCH, CIP and doxycycline (DOX) within 30 min.

In view of the stability and conductivity of noble metals, Ag, Pd, Au, Rh and Pt nanoparticles have been used to decorate BiOX. In this field, Yu *et al.*[113] selectively deposited Ag nanoparticles on different surface regions of BiOCl single-crystal nanosheets, and compared the photocatalytic activity of different Ag/BiOCl samples. The Ag/BiOCl-(UV) sample with Ag nanoparticles deposited on exposed {001} facets presented the highest photocatalytic activity for degradation of MO and phenol, much better that the sample with Ag deposited on the lateral surfaces of BiOCl and the sample with Ag nanoparticles randomly deposited on BiOCl. In addition, Ag and Bi loaded BiOCl (Ag/Bi/BiOCl) microflowers were synthesized by *in situ* solvothermal method for degradation of Rh B.[114] Coexistence of Ag, Bi nanoparticles and oxygen vacancies enhanced the light absorption range and promoted the charge-carrier separation. Therefore, the Ag/Bi/BiOCl showed a higher photocatalytic activity than that of P25 and pure BiOCl under visible light and UV irradiation. Meng *et al.*[115] synthesized palladium (Pd) nanoparticles on BiOBr surface *via* electrostatic assembly method. A Mott–Schottky junction formed between Pd and BiOBr promoted the separation of photogenerated carriers. Furthermore, the synergetic effect between SPR and Mott–Schottky junction contributed to the enhanced photocatalytic activity for removal of phenol under visible light. Li *et al.*[116] synthesized Au–BiOCl and Pd–BiOCl photocatalysts by loading Au or Pd nanoparticles on ultrathin BiOCl (001) nanosheets for oxidation of benzyl alcohol. After decorating with noble metal nanoparticles, much more oxygen vacancies and active sites

were introduced into BiOCl nanosheets, which facilitated the adsorption and activation of alcohols. Moreover, strong interface cooperation was formed between Pd and BiOCl (001) surface by the electronic coupling. The strong surface activity of Pd nanoparticles and abundant oxygen vacancies on BiOCl (001) synergistically improved the adsorption-activation of alcohol molecules and O_2, which enhanced the photocatalytic activity of BiOCl. In addition, noble metals (Rh, Pd, Pt)-deposited BiOX (Cl, Br, I) photocatalysts were synthesized *via* solution-photodeposition method.[117] Decorated Pd and Pt existed in metallic state, while Rh existed in both metallic and oxidized states. The decoration of three noble metals reduced the band gaps and inhibited the recombination of the electron–hole pairs. Under the irradiation of UV light, the descending activity order was Pd(0.5%)/BiOBr > Pt(1%)/BiOCl > Pd(2%)/BiOCl. Under the visible light, the activity order changed to Pd(4%)/BiOBr > Pd(0.5%)/BiOI > Rh(1%)/BiOCl.

3.2.5 Decoration with carriers. Oxidized cellulose nanofibrils (CNFs) contain abundant carbonyls and hydroxyls, which can be served as active sites to adsorb organic dyes. By using oxidized CNFs as a regulator, Tian *et al.*[118] synthesized CNFs-decorated flower-like BiOCl with hydrophilic surface. The composite containing 5% CNFS displayed the highest photodegradation rate for removal of Rh B and TC under visible light. In addition, acidized sepiolite (AS) and polyvinyl pyrrolidone (PVP) were used to modify BiOBr hierarchical microspheres for degradation of Rh B and diclofenac sodium.[119] As-prepared PVP/AS/BiOBr photocatalyst with 6% AS had a hollow spherical structure (Fig. 6a), which exhibited a superior photocatalytic activity for the enhanced light adsorption range and the fast separation of photogenerated electron–hole pairs. Polyaniline (PANI) has a high charge transfer capability and high absorption ability in the visible light,[120] which can be acted as an excellent electron donor. PANI-modified BiOI was prepared *via* co-precipitation method.[121] The loading of PANI on BiOI enhanced the separation efficiency of electron–hole pairs, and the PANI/BiOI composite with 12.5 wt% PANI achieved a high removal efficiency of 91% for degradation of Rh B under visible light. Xu *et al.*[122] synthesized polypyrrole (Ppy) decorated BiOI *via in situ* precipitation method. The decoration of Ppy generated abundant active sites, and increased the specific surface area, which facilitated the transfer and separation of photogenerated charge carriers. Therefore, Ppy-BiOI composite exhibited an enhanced photocatalytic activity for degradation of Rh B, bisphenol A, 2,4-dichlorophenol, tetracycline hydrochloride and chlortetracycline hydrochloride.

Cui *et al.*[123] synthesized I-deficient BiOI thin film on glass substrate *via* a solvothermal method under the assistance of ([C6Mim]I) ionic liquid. The calcinations of BiOI-coated substrate produced I-deficient BiOI. The iodine vacancies effectively trapped the photogenerated holes, which inhibited the recombination of photogenerated electron–hole pairs. Therefore, the I-deficient BiOI thin film displayed a superior photocatalytic performance for degradation of BPA, and a good reusability for practical wastewater treatment. Ge *et al.*[124] synthesized BiOBr on superhydrophobic Cu mesh, and BiOBr-decorated Cu mesh exhibited an excellent cycling stability for degradation of Rh B, MB and ciprofloxacin drug. In addition,

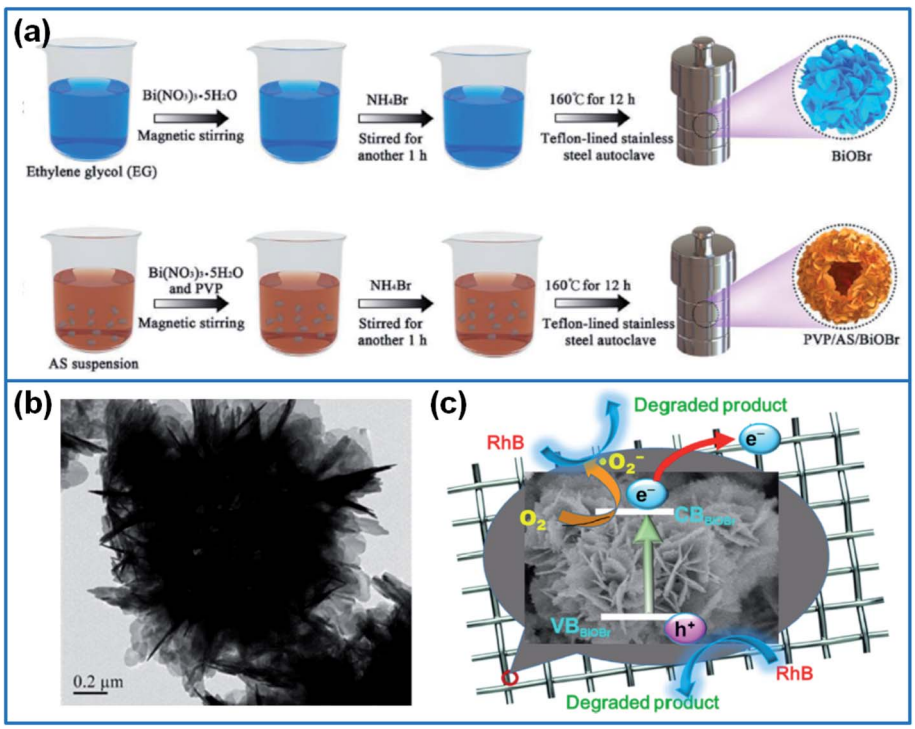

Fig. 6 (a) Schematic illustration for preparing BiOBr and PVP/AS/BiOBr composite.[119] Copyright 2019 Elsevier. (b) TEM image of flower-like BiOBr, and (c) photodegradation mechanism of Rh B dye by loading BiOBr on metal wire mesh.[125] Copyright 2019 Elsevier.

Chang *et al.*[125] synthesized flower-like BiOBr on stainless steel wire mesh *via* solvothermal method and calcinations (Fig. 6b and c). After heated at 250 °C, the (001) facets of BiOBr were generated, which reduced the energy gap and enhanced the photocurrent density. The metal mesh/BiOBr showed an enhanced photocatalytic activity for degradation of Rh B.

3.3. Summary

To sum up, the doping and surface modification of BiOX was summarized in this section. The heteroatom doping effectively adjusts the band gap of BiOX and promotes the transfer and separation of photogenerated electron–hole pairs. Among non-metal elements, boron (B), carbon (C), nitrogen (N), sulfur (S) and iodine(I) have been reported as dopants for improving the photocatalytic activity of BiOX. However, up to now, there are no related reports about Si, P, and F doped BiOX, which would become a promising research direction. Besides non-metal dopants, metal dopants including normal metals (Al, Zn, Sn, In, and Pt), transition metals (Co, Fe, Ti, Mn, W, and Nb), and lanthanides metals (La, Ce, Y, Yb, and Er), have been reported for preparing doped BiOX. In view of the up-conversion luminescence of lanthanides ions, Ln-doped BiOX displayed an outstanding photocatalytic activity. However, considering the high cost of rare earth elements, some transition metals show obvious advantage for the high performance and low cost. In addition, dual doping by non-metal and metal or two metals also exhibits an excellent performance for playing the synergistic effect. In addition, surface modification of BiOX involves much more research contents, such as, generation of surface defects or oxygen vacancies, introduction of active sites or hydroxyl groups, decoration with inorganic/organic frameworks, carbon materials, metal particles, and other carriers, and so on. Some metal decorators or conductive carriers have been widely reported to improve the photocatalytic performance of BiOX. In consideration of the reusability in wastewater treatment, free-standing Cu mesh decorated with BiOX shows a promising application prospect for the simple post-treatment.

4. Heterojunction of different compounds

Besides heteroatom doping and surface modification, the construction of heterojunction is widely reported for enhancing the photocatalytic activity of single-component BiOX. Compared to single BiOX, the combination of different BiOX species effectively adjusts the band gap energy and increases the visible light absorption capability. Furthermore, the heterojunction achieves the fast transfer of electrons and holes, suppresses the recombination of electron–hole pairs, and enhances the photocatalytic activity. In this section, we classify the BiOX heterojunction into two parts. The first is BiOX/BiOY type heterojunction, including BiOCl/BiOBr, BiOCl/BiOI, BiOBr/BiOI, BiOF/BiOBr, and some ternary composites containing BiOX/BiOY. The second is BiOX/$Bi_mO_nX_z$ type heterojunction.

4.1. BiOX/BiOY heterojunction

Due to the structure similarity of BiOCl and BiOBr, one-step hydrothermal or solvothermal method was used to prepare BiOCl/BiOBr heterojunction, and the morphology and the ratio of BiOCl/BiOBr are the main factors for deciding the photocatalytic activity. In this field, Cui *et al.*[126] synthesized BiOCl nanoparticles on BiOBr nanosheets *via* hydrothermal method, and the BiOBr/BiOCl hybrid nanosheets with the weight ratio of 10 : 1 exhibited the best photocatalytic activity for degradation of Rh B. Under the assistance of ethylene glycol (EG), Zhang *et al.*[127] prepared nanosheet-assembled BiOCl/BiOBr microspheres (Fig. 7a). Through adjusting the ratio of BiOBr/BiOCl, the composite of 40% BiOCl/BiOBr displayed the best photocatalytic efficiency for degradation of MB under LED light. In addition, 3D hierarchical microspheres of BiOBr/BiOCl were prepared by solvothermal method.[128] The BiOBr/BiOCl composite with the mole ratio of 2 : 3 presented the best photodegradation performance for degradation of Rh B, and the degradation rate constant was 4.5 times and 8.8 times higher than pure BiOBr and pure BiOCl, respectively. Li *et al.*[129] synthesized flower-like BiOBr/BiOI composite *via* solvothermal method and discussed the effect of BiOBr/BiOI molar ratios on the degradation efficiency. The composite with BiOBr/BiOI ratio of 3 : 1 delivered the highest degradation activity, which degraded 99.8% Rh B in 80 min under visible light. Jiang *et al.*[130] prepared BiOBr/BiOF composites with different Br/F ratios. As shown in Fig. 7b, the introduction of BiOF reduced the crystalline size and suppressed the recombination of electron–hole pairs, and the synergistic effect between BiOF and BiOBr enhanced the photocatalytic activity for degradation of Rh B and nitrobenzene.

Compared to inorganic KCl, KBr or KI precursors, Cl-, Br- or I-containing ionic liquids can be served as precursor, solvent and template for synthesizing BiOX. Under the presence of 1-hexadecyl-3-methylimidazolium chloride ([C16mim]Cl) and 1-hexadecyl-3-methylimidazolium bromide ([C16mim]Br) ionic liquids, Zhang *et al.*[131] synthesized BiOCl/BiOBr flower-like microspheres *via* solvothermal method. This composite achieved the complete decomposition of Rh B, due to the excellent visible light absorption capability. In addition, Yang *et al.*[132] synthesized flower-like BiOBr/BiOCl heterojunction by using 1-allyl-3-methylimidazolium bromide ([AMIm]Br) ionic liquid and KCl as reactants. When used for degradation of Rh B, the photocatalytic performance of BiOBr/BiOCl composite was six times higher than that of pure BiOCl. By using 1-propyl-3-methylimidazolium iodide ([PrMIm]I) ionic liquid (IL) as solvent and I source, Liu *et al.*[133] prepared BiOI/BiOCl heterojunction photocatalysts *via* a hydrothermal method. Compared to pure BiOCl and BiOI, BiOI/BiOCl heterojunction presented a higher separation efficiency of photo-generated charge pairs. When the mass ratio of [PrMIm]I/BiOCl is 8%, the composite showed the highest photocatalytic activity for degradation of Rh B under simulated sunlight, and the degradation rate was 7.7 and 5.8 times higher than that of BiOCl and BiOI.

In addition, self-assembled BiOI/BiOCl microflowers[134] and hierarchical porous flower-like BiOI/BiOCl composite were

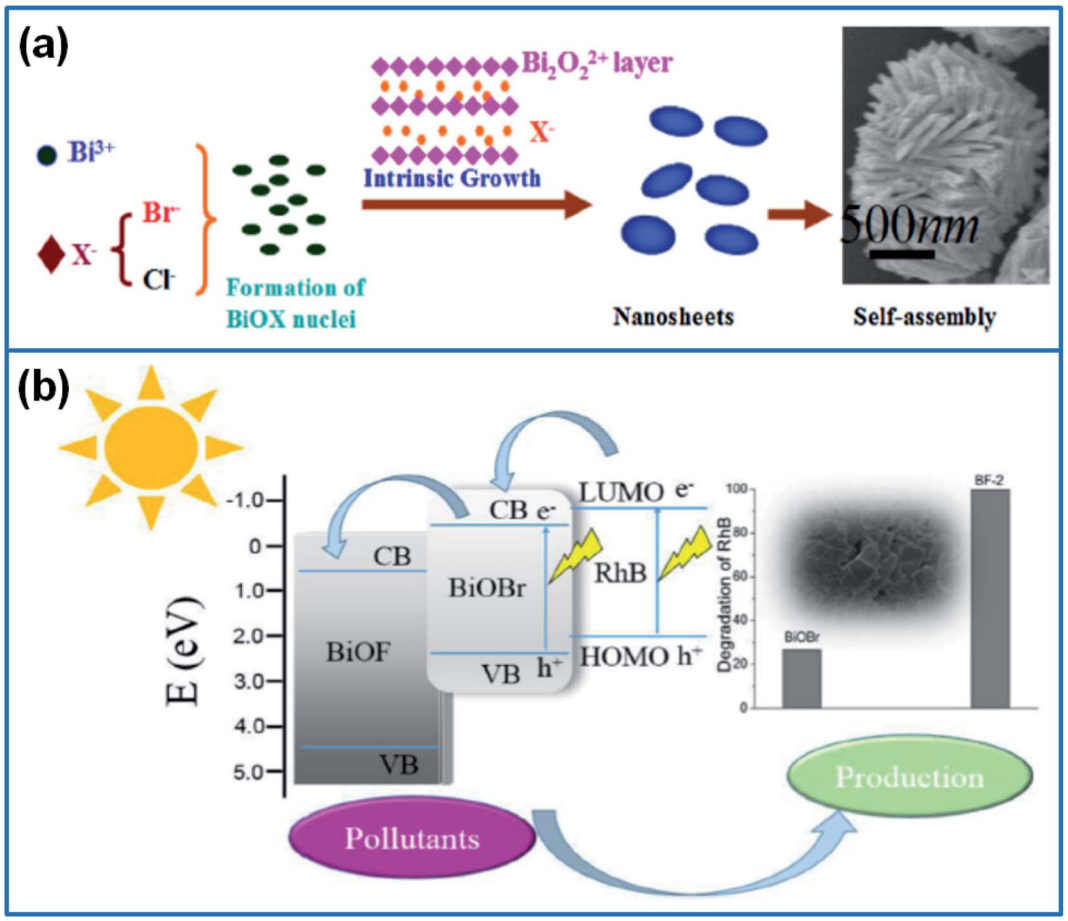

Fig. 7 (a) Schematic illustration for fabricating BiOCl/BiOBr microsphere.[127] Copyright 2018 Elsevier. (b) Schematic illustration of the charge transfer and separation of BiOBr/BiOF heterojunction.[130] Copyright 2017 Elsevier.

synthesized by a template-free method.[135] In this hierarchical porous BiOI/BiOCl composite, tri-model mesopores were formed by the aggregation of self-assembled nanoplates. Due to the large surface area and pore volume, and modified band structure, this composite displayed an enhanced visible light activity for removal of NO in air.

Besides hydrothermal or solvothermal method, microwave-assisted precipitation method was used to synthesize BiOCl/BiOBr composite.[136] Through adjusting the molar ratios of Cl/Br, the 1 : 5 BiOCl/BiOBr composite presented the best visible-light photocatalytic activity for degradation of Rh B, due to the strong visible light absorption capability and the low recombination rate of electron–hole pairs. Through doping with I^- ions, flower-like I-BiOCl/I-BiOBr composite was synthesized by a deposition–precipitation method.[137] The doping of I^- ions not only enhanced the visible light absorption capability of BiOCl and BiOBr, but also formed type-II heterojunction through adjusting their energy level of valence bands. Due to the strong visible light absorption and efficient separation of electrons and holes, the 20% I-BiOCl/I-BiOBr composite displayed the highest photocatalytic activity for degradation of MO and phenol under visible light.

In addition, Lin *et al.*[138] synthesized BiOI/BiOBr composite photocatalyst *via* a facile anion-exchange method through replacing partial of Br^- by I^-. The BiOI/BiOBr heterojunction presented much higher photocurrent intensity than pristine BiOI and BiOBr, which contributed to the higher photocatalytic activity for degradation of MO dye under visible light. Jamil *et al.*[139] synthesized $BiOI_{0.5}Br_{0.5}$ heterojunction by a facile chemical etching method. When used for degradation of Lindane pesticide, the heterojunction presented much higher photocatalytic activity than pure BiOBr and BiOI. Bai *et al.*[140] prepared $BiOBr_xI_{1-x}$/BiOBr heterojunction photocatalyst by coupling $BiOBr_xI_{1-x}$ with BiOBr monomer. The $BiOBr_xI_{1-x}$/BiOBr exhibited a high molecular oxygen activation capacity, which enhanced the photocatalytic performance for degradation of Rh B, phenol and BPA under visible light.

Oxygen vacancies (OVs) could increase the surface dangling bonds and active sites on the BiOX. Moreover, the defects induced by OVs effectively suppress the recombination of electron–hole pairs.[141] In view of the function of OVs, Liu *et al.*[142] synthesized BiOCl/BiOBr heterojunction with rich OVs *via* ultrasound and photoinduced method. Abundant OVs in BiOCl/BiOBr provided active sites for photocatalytic reaction, and enhanced the light absorption range. Furthermore, the

interface electric field derived from BiOCl/BiOBr heterostructure accelerated the electron transfer and inhibited the recombination of photogenerated electron–hole pairs. Therefore, the composite presented a high photocatalytic activity for degradation of carbamazepine under visible light. In addition, under the assistance of PVP K30, ultrathin BiOBr/BiOI (BiOBr/BiOI-U) photocatalyst with OVs was synthesized *via* a solvothermal method,[143] and the BiOBr/BiOI-U composite exhibited high photocatalytic efficiency for removal of NO.

Besides abundant experimental studies, density functional calculations were adopted to investigate the structural, electronic, and optical properties of BiOX/BiOY heterojunction systems, including BiOF, BiOCl, BiOBr, and BiOI.[144] The results confirmed that all the BiOX/BiOY superlattice systems were indirect bandgap semiconductors, and the bandgap of BiOX/BiOY system was between two bandgap values of BiOX and BiOY. The maximum absorption wavelength had a sequence of BiOF < BiOF/BiOCl < BiOCl < BiOF/BiOBr < BiOCl/BiOBr < BiOBr < BiOF/BiOI < BiOCl/BiOI < BiOBr/BiOI < BiOI. The bandgap of BiOF/BiOI, BiOCl/BiOBr, BiOCl/BiOI, and BiOBr/BiOI was 2.74, 2.99, 2.30, and 2.23 eV, respectively. The performance comparison of different heterojunctions provided guidelines for the design of high-active heterojunctions.

In order to further improve the activity of BiOX heterojunction, some carriers or decorators, such as, conductive carbon materials, cellulose, noble metal and stainless steel wire mesh have been used for preparing ternary composites. Among carbon materials, carbon quantum dots (CQDs) has superior electron transfer/reservoir properties, and photoluminescence (PL) up-conversion effect, which can be used to expand the light utilization range and promote photo-induced electron transfer.[145] Zhao *et al.*[146] synthesized BiOBr/BiOCl/CQDs heterostructure microspheres *via* a solvothermal method. When used for degradation of Rh B, the BiOBr/BiOCl/CQDs-4% exhibited a high photocatalytic activity under visible light, and the photodegradation rate was 2.8 times higher than that of BiOBr/BiOCl, due to the strong light harvesting capacity and outstanding electron transferability between BiOCl and CQDs. Besides CQDs, Su *et al.*[147] synthesized BiOCl/BiOI flower-like hollow microspheres on rGO sheets for photodegradation of Rh B. The introduction of GO changed the morphology of 50% BiOCl/BiOI from solid microspheres to hollow microspheres, which enhanced the light absorption. Moreover, the high conductivity of rGO and the strong interfacial interaction between rGO and BiOCl/BiOI effectively promoted the separation of photogenerated carriers. Therefore, the incorporation of rGO showed over twice degradation rate than that of pristine 50% BiOCl/BiOI under visible light.

Due to the remarkable compatibility between cellulose and BiOBr/BiOI, Du *et al.*[148] prepared BiOBr/BiOI/cellulose composite by using pulp board as the cellulose source. Meanwhile, the combination of three components broadened the visible light absorption, and improved the migration efficiency of the electron–holes. So BiOBr/BiOI/cellulose composite displayed a high degradation activity for removal of Rh B, fluorescein dye (FL) and TCH under visible light.

Considering the function of noble metal in improving the photocatalytic activity, Ren *et al.*[149] developed flower-like Pd/BiOCl/BiOI photocatalyst *via* a solvothermal method. The deposition of Pd on BiOCl/BiOI suppressed the recombination of photoinduced electrons and holes, and enhanced the photodegradation performance. The composite of 3% Pd/BiOCl/BiOI displayed the best photocatalytic activity for degradation of Rh B under the irradiation of 350 W Xe lamp. In order to improve the reusability of photocatalysts, Wang *et al.*[150] prepared BiOI/BiOBr heterostructure film on 304 stainless steel wire mesh. The free-standing composite film prepared with 50 mM TBAB exhibited high photodegradation efficiency for removal of Rh B. Meanwhile, this heterostructure film showed high mechanical strength and cycling stability.

4.2. BiOX/$Bi_mO_nX_z$ heterojunction

In the family of bismuth oxyhalide, besides the BiOX (X = F, Cl, Br, I), newly discovered non-stoichiometric bismuth oxyhalides ($Bi_mO_nX_z$) have been reported, such as, $Bi_{24}O_{31}Br_{10}$,[151] $Bi_{12}O_{17}Cl_2$,[152] Bi_3O_4Br,[153] Bi_5O_7I,[154] and $Bi_{12}O_{15}Cl_6$.[155] Recently, BiOX/$Bi_mO_nX_z$ composites have been developed for enhancing the photocatalytic activity. In this field, a novel 3D flower-like Bi_3O_4Cl/BiOCl heterostructure was prepared by a co-precipitation method for degradation of antibiotic drug.[156] The composite exhibited a high photocatalytic activity in visible light range for the efficient charge-separation properties, which degraded 87% levofloxacin in 180 min. In addition, mesoporous-mixed-phase bismuth oxychlorides was fabricated by using one-pot sorbitol-nitrate solution autocombustion method,[157] and the intra-heterojunction containing 59% BiOCl and 41% $Bi_{24}O_{31}Cl_{10}$ displayed a high activity for degradation of antibiotic ofloxacin, due to the enhanced light absorption and surface reactions by a high porosity.

Liu *et al.*[158] synthesized Bi_3O_4Br/BiOCl heterojunction photocatalyst. The composite presented a high photocatalytic activity in degradation of Rh B, and the degradation rate was 6.3 and 3.1 times higher than that of pure Bi_3O_4Br and BiOCl. Wang *et al.*[159] prepared heterostructured 2D/2D BiOBr/$Bi_{12}O_{17}Cl_2$ photocatalysts *via* a chemical deposition–precipitation method (Fig. 8a). The BiOBr/$Bi_{12}O_{17}Cl_2$ heterostructure presented a high photocatalytic activity for degradation of MO, 4-chlorophenol (4-CP) and TC under visible light. Heidari *et al.*[160] synthesized 3D-flower-like BiOCl/BiOBr/$Bi_{24}O_{31}Br_{10}$ composite *via* sono-assisted solvothermal method (Fig. 8b). The generated type-II heterojunction enhanced the photocatalytic activity for removal of levofloxacin, ofloxacin, norfloxacin and ciprofloxacin.

Sun *et al.*[161] synthesized $Bi_4O_5Br_xI_{2-x}$ photocatalysts by a facile precipitation method, and discussed the influence of I/Br molar ratio on the photocatalytic performance. When used for decomposing resorcinol, *o*-phenylphenol, and 4-*tert*-butylphenol, the $Bi_4O_5Br_{0.6}I_{1.4}$ sample presented the best activity, due to the enhanced charge separation efficiency and enlarged visible light absorption. In another work, Du *et al.*[162] synthesized $BiOCl_xBr_{1-x}$ sheets with different Cl/Br ratios *via* a precipitation method, and the composite with Cl/Br ratio of

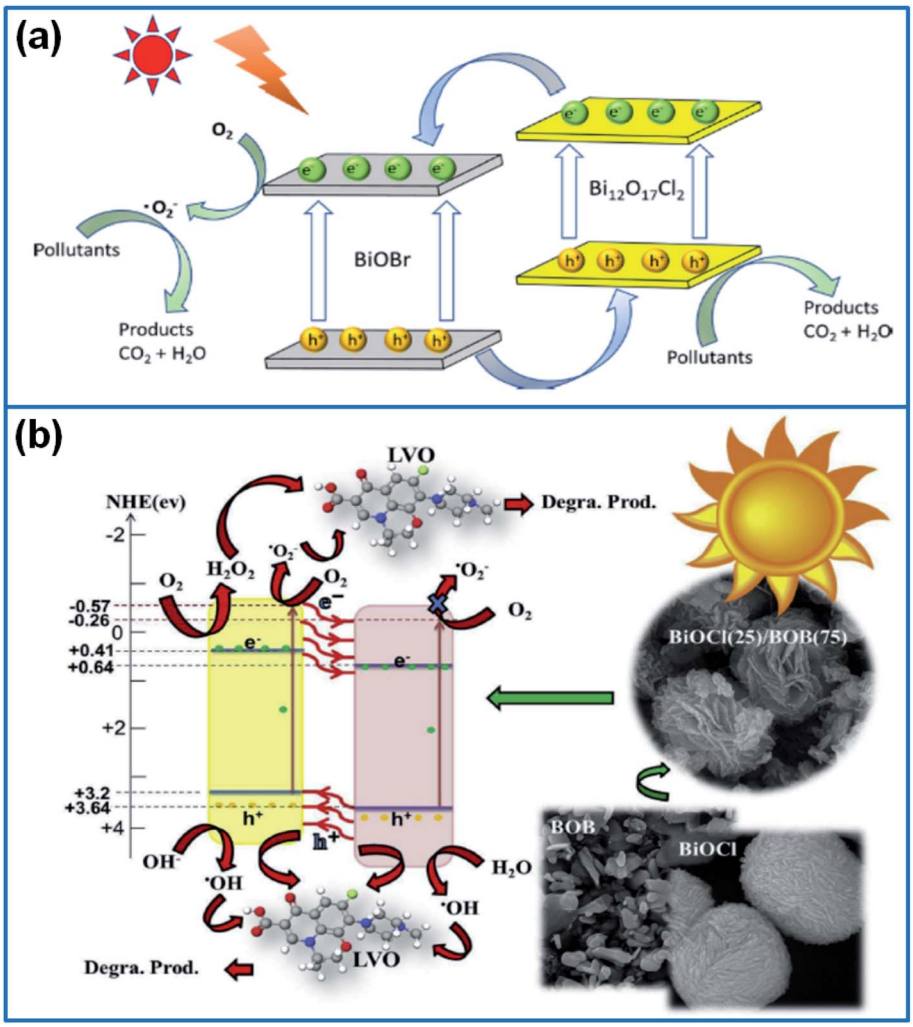

Fig. 8 (a) Schematic illustration for the transport and separation of the photo-induced electron–hole pairs and the degradation mechanism of BiOBr/$Bi_{12}O_{17}Cl_2$ composite.[159] Copyright 2020 Elsevier. (b) Degradation mechanism for removal of levofloxacin by using 3D flower-like BiOCl(25)/BOB(75) heterojunction photocatalysts.[160] Copyright 2020 Elsevier.

1 : 1 presented the highest activity for degradation of Rh B. The degradation ratio reached 99% in 30 min under visible light irradiation. Moreover, Xu *et al.*[163] confirmed that the $BiOCl_{0.5}Br_{0.5}$ nanoplates had the highest photocatalytic activity for degradation of Rh B under simulated sunlight. Considering the influence of microstructure on the photocatalytic activity, Kim *et al.*[164] synthesized 3D flower-like and 2D plate-like $BiOCl_xI_{1-x}$ with different Cl/I ratios respectively. With an increase of I content, the specific surface area and adsorption ability of $BiOCl_xI_{1-x}$ greatly increased. When used for degradation of MO and Rh B under visible light, the sample with flower-like structure showed a better adsorption and photodegradation performance than 2D plate-like structure.

4.3. Summary

In order to further enhance the photocatalytic activity of single-component BiOX, the heterojunction of BiOX have been widely developed in recent years. According to the component of heterojunction, we classify the BiOX heterojunction into BiOX/BiOY and BiOX/$Bi_mO_nX_z$ type heterojunction. In the section of BiOX/BiOY heterojunction, BiOCl/BiOBr, BiOCl/BiOI, BiOBr/BiOI, and BiOBr/BiOF, have been summarized and applied for degradation of organic pollutants. The selection of halide and their ratio are the research topics for deciding the photocatalytic activity. Moreover, some carriers or decorators including carbon quantum dots, rGO, cellulose, noble metal Pd and stainless steel wire mesh, have been hybridized with BiOX/BiOY heterojunction. These decorated heterojunctions usually exhibit superior electron transfer/separation properties and visible light absorption ability. The results confirm that the decoration of BiOX/BiOY heterojunction is another effective way for enhancing the photocatalytic activity. Different from BiOX, $Bi_mO_nX_z$ has different ratios of Bi/O/X, abundant active sites and oxygen vacancies, which facilitate the enhancement of photocatalytic activity. There are more types of $Bi_mO_nX_z$ species, such as, $Bi_{24}O_{31}Br_{10}$, $Bi_{12}O_{17}Cl_2$, Bi_3O_4Br, Bi_3O_4Br, $BiOCl_xBr_{1-x}$, $BiOCl_xI_{1-x}$, $Bi_4O_5Br_xI_{2-x}$, and so on. When hybridized with these special $Bi_mO_nX_z$ species, the BiOX/$Bi_mO_nX_z$

heterojunctions present outstanding photocatalytic activity for removal of organic dyes and pharmaceuticals, even better than traditional BiOX/BiOY heterojunction. Therefore, developing novel $Bi_mO_nX_z$ species and BiOX/$Bi_mO_nX_z$ heterojunctions is a promising prospect for designing high-performance BiOX photocatalysts.

5. Conclusions and prospects

In view of the important role of BiOX in semiconductor photocatalysts, herein, we summarize the recent advances on BiOX photocatalysts, including the controllable synthesis, doping and surface modification, and heterojunction of different BiOX species. Crystal structure, size and specific surface area are the main factors for deciding the photocatalytic activity of BiOX. While synthetic methods decide the physical properties of BiOX, so the synthetic methods of BiOX are introduced firstly, in which, seven methods are classified, including hydrothermal, solvothermal, hydrolysis method, precipitation method, two-phase method, ultrasonic/microwave-assisted method and physical method. Among these synthetic methods, hydrothermal and solvothermal method are most popular for the uniform morphology and easy operation. In the hydrothermal/solvothermal reaction, reaction conditions (temperature and time), halide precursors, surfactants, and solvent systems greatly affect the microstructure and performance of BiOX. The preferred morphology is thin BiOX nanosheets with highly exposed (010) facets, or hierarchical BiOX spheres/flowers with a large specific surface area. In addition, microwave-assisted method can be adopted to shorten the reaction time and improve production efficiency. Compared to solution-based synthetic methods, calcinations method and mechanical grinding method show some advantages in the industrial-scale production. In the second part, we introduce the doping and surface modification of BiOX. The doping is introducing heteroatoms into the crystal planes of BiOX, which effectively adjusts the band gap and enhances the visible light absorption capability. The doping elements and doping dosage greatly affect the photocatalytic activity of BiOX. Various non-metal elements, including B, C, N, S and I, have been used for doping different BiOX species. Compared to non-metals, metal elements including Al, Zn, Sn, In, Pt, Co, Fe, Ti, Mn, W, Nb, and lanthanides metal (La, Ce, Y, Yb, and Er) have been reported for preparing metal-doped BiOX. In addition, dual-doping has been reported by introducing non-metal and metal or two metals, such as, Bi quantum dots implanted C-doped BiOCl, Ag and carbon dots co-doped BiOI microspheres, Fe and N co-doped BiOBr, Fe, Nb co-doped BiOCl, Er^{3+} an Yb^{3+} ions doped BiOCl, and Ho^{3+}/Yb^{3+} and Er^{3+}/Yb^{3+} co-doped BiOCl. Compared to non-metal doping or metal doping, dual doping of BiOX achieves the synergistic effect of two dopants. Moreover, dual-doping provides much more choices for developing novel doped BiOX. Different from heteroatom doping, surface modification introduces different surface terminations on the surface of BiOX, or decorate BiOX with different carriers. For example, alcohols or amines modified BiOX exhibits a good hydrophilic feature, which facilitates the adsorption of organic molecules. Furthermore, oxygen vacancies or defects generated on BiOX would greatly enhance the photocatalytic activity. Various carriers, including inorganic/organic frameworks, carbon materials, metal nanoparticles, cellulose, sepiolite, conductive polymers, glass substrate, metal mesh have been reported for loading BiOX photocatalysts. The decoration not only adjusts the microstructure, increases the specific surface area of BiOX, but also promotes the transfer and separation of photogenerated carriers and charges, further enhancing the photocatalytic performance. Among the carriers, free-standing Cu mesh can be used for preparing self-supporting photocatalysts, which exhibits an excellent reusability in wastewater treatment. In the third section, different BiOX heterojunctions are summarized, including BiOX/BiOY heterojunction and BiOX/$Bi_mO_nX_z$ heterojunction. In the field of BiOX/BiOY heterojunctions, BiOCl/BiOBr, BiOCl/BiOI, BiOBr/BiOI, and BiOBr/BiOF have been synthesized and applied for degradation of organic dyes and antibiotics. The halide types and their ratio of BiOX/BiOY greatly affect the photocatalytic performance. Furthermore, some carriers or decorators including carbon quantum dots, rGO, cellulose, noble metal Pd and stainless steel wire mesh, have been hybridized with BiOX/BiOY heterojunction to fabricate ternary composite photocatalysts. These ternary composites exhibit superior electron transfer/separation properties and visible light absorption ability, much better than that of BiOX/BiOY. Different from BiOX, $Bi_mO_nX_z$ has different ratios of Bi/O/X. Abundant active sites and oxygen vacancies enable the $Bi_mO_nX_z$ with much higher photocatalytic activity. Up to now, $Bi_{24}O_{31}Br_{10}$, $Bi_{12}O_{17}Cl_2$, Bi_3O_4Br, Bi_3O_4Br, $BiOCl_xBr_{1-x}$, $BiOCl_xI_{1-x}$ and $Bi_4O_5Br_xI_{2-x}$, have been reported for hybridizing with BiOX, and exhibit a superior photocatalytic activity.

Up to now, a great progress has been achieved in the field of BiOX photocatalysts. However, there are some tough problems to be solved, such as, the controllable synthesis of BiOX, most efficient modification method, and the relationship between the microstructure and photocatalytic activity. These existing problems just provide potential research directions, which can be summarized as following:

(1) Developing novel synthetic methods for preparing BiOX photocatalysts with particular microstructures. The preferred morphologies include hierarchical flowers/spheres with high specific surface area, ultrathin nanosheets with highly exposed {001} facets, and hollow nanostructure. In addition, the cost of raw materials, preparation periods and mass-production are the essential factors for consideration.

(2) Effective doping or modification on the facet or surface of BiOX. Heteroatom doping and surface modification are effective strategies for enhancing the photocatalytic activity of BiOX. Based on existing reports, the main tasks are developing dual-doped BiOX and selecting suitable carriers for hybridizing with BiOX.

(3) Developing novel $Bi_mO_nX_z$ species and BiOX/$Bi_mO_nX_z$ heterojunctions. $Bi_mO_nX_z$ displays much higher photocatalytic activity than traditional BiOX for rich active sites and oxygen vacancies. Therefore, developing novel $Bi_mO_nX_z$ species and BiOX/$Bi_mO_nX_z$ heterojunctions is a promising research topic.

(4) Disclosing the relationship between microstructure and photocatalytic performance. Theory computation about the band gap and energy level of BiOX would provide theoretical instruction for designing the microstructure and selecting suitable matching component. Therefore, the combination of experiment and computation is essential for developing BiOX-based photocatalyts.

At last, photocatalysis is an environmental-friendly strategy for solving the wastewater problem. In view of the high photocatalytic activity of BiOX, the development of BiOX-based photocatalysts is becoming a major task in photocatalytic field, which would greatly promote the development of environmental protection industries.

Conflicts of interest

There are no conflicts to declare.

Acknowledgements

This research was supported by National Natural Science Foundation of China (No. 51403094).

References

1 X. Wei, M. U. Akbar, A. Raza and G. Li, *Nanoscale Adv.*, 2021, **3**, 3353.
2 J. Di, J. Xia, H. Li, S. Guo and S. Dai, *Nano Energy*, 2017, **41**, 172.
3 P. Raizada, A. Sudhaik, P. Singh, P. Shandilya, V. K. Gupta, A. Hosseini-Bandegharaei and S. Agrawal, *J. Photochem. Photobiol., A*, 2019, **374**, 22.
4 P. Singh, P. Shandilya, P. Raizada, A. Sudhaik, A. Rahmani-Sani and A. Hosseini-Bandegharaei, *Arabian J. Chem.*, 2020, **13**, 3498.
5 A. Kumar, P. Raizada, P. Singh, R. V. Saini, A. K. Saini and A. Hosseini-Bandegharaei, *Chem. Eng. J.*, 2020, **391**, 123496.
6 P. Raizada, A. Sudhaik, P. Singh, A. Hosseini-Bandegharaei and P. Thakur, *Sep. Purif. Technol.*, 2019, **227**, 115692.
7 V. Dutta, P. Singh, P. Shandilya, S. Sharma, P. Raizada, A. K. Saini, V. K. Gupta, A. Hosseini-Bandegharaei, S. Agarwal and A. Rahmani-Sani, *J. Environ. Chem. Eng.*, 2019, **7**, 103132.
8 L. Ye, Y. Su, X. Jin, H. Xie and C. Zhang, *Environ. Sci.: Nano*, 2014, **1**, 90.
9 A. Kumar, P. Raizada, V. Kumar Thakur, V. Saini, A. Aslam Parwaz Khan, N. Singh and P. Singh, *Chem. Eng. Sci.*, 2021, **230**, 116219.
10 G. Boczkaj and A. Fernandes, *Chem. Eng. J.*, 2017, **320**, 608–633.
11 A. Kumar, P. Raizada, A. Hosseini-Bandegharaei, V. K. Thakur, V. H. Nguyen and P. Singh, *J. Mater. Chem. A*, 2021, **9**, 111.
12 Sonu, V. Dutta, S. Sharma, P. Raizada, A. Hosseini-Bandegharaei, V. Kumar Gupta and P. Singh, *J. Saudi Chem. Soc.*, 2019, **23**, 1119.
13 J. Zhan, J. Wu, P. Lu, Q. Liu, T. Huang, H. Tian, R. Zhou, J. Ren, B. Yuan and X. Sun, *Mater. Lett.*, 2017, **186**, 353–356.
14 X. Zhang, R. Li, M. Jia, S. Wang, Y. Huang and C. Chen, *Chem. Eng. J.*, 2015, **274**, 290–297.
15 P. Intaphong, A. Phuruangrat, K. Karthik, P. Dumrongrojthanath, T. Thongtem and S. Thongtem, *J. Inorg. Organomet. Polym.*, 2020, **30**, 714–721.
16 H. Feng, Z. Xu, L. Wang, Y. Yu, D. Mitchell, D. Cui, X. Xu, J. Shi, T. Sannomiya and Y. Du, *ACS Appl. Mater. Interfaces*, 2015, **7**, 27592–27596.
17 L. Dou, D. Ma, J. Chen, J. Li and J. Zhong, *J. Solid State Sci.*, 2019, **90**, 1–8.
18 Z. Zou, H. Xu, D. Li, J. Sun and D. Xia, *Appl. Surf. Sci.*, 2019, **463**, 1011–1018.
19 K. Li, Y. Liang, J. Yang, Q. Gao, Y. Zhu, S. Liu, R. Xu and X. Wu, *J. Alloys Compd.*, 2017, **695**, 238–249.
20 Y. Cai, D. Li, J. Sun, M. Chen, Y. Li, Z. Zou, H. Zhang, H. Xu and D. Xia, *Appl. Surf. Sci.*, 2018, **439**, 697–704.
21 X. Gao, W. Peng, G. Tang, Q. Guo and Y. Luo, *J. Alloys Compd.*, 2018, **757**, 455–465.
22 J. Tian, Z. Chen, X. Deng, Q. Sun, Z. Sun and W. Li, *Appl. Surf. Sci.*, 2018, **453**, 373–382.
23 A. C. Mera, H. Váldes, F. J. Jamett and M. Meléndrez, *Solid State Sci.*, 2017, **65**, 15–21.
24 A. C. Mera, Y. Moreno, D. Contreras, N. Escalona, M. F. Meléndrez, R. V. Mangalaraja and H. D. Mansilla, *Solid State Sci.*, 2017, **63**, 84–92.
25 Z. Jiang, X. Liang, Y. Liu, T. Jing, Z. Wang, X. Zhang, X. Qin, Y. Dai and B. Huang, *Appl. Catal., B*, 2017, **211**, 252–257.
26 X. Zhang, C. Y. Wang, L. W. Wang, G. X. Huang, W. K. Wang and H. Q. Yu, *Sci. Rep.*, 2016, **6**, 1–10.
27 H. Zhao, X. Liu, Y. Dong, Y. Xia and H. Wang, *Appl. Catal., B*, 2019, **256**, 117872.
28 X. Gao, Q. Guo, G. Tang, W. Zhu and Y. Luo, *J. Solid State Chem.*, 2019, **277**, 133–138.
29 H. Xing, H. Ma, Y. Fu, X. Zhang, X. Dong and X. Zhang, *J. Renewable Sustainable Energy*, 2015, **7**, 063120.
30 X. X. Wei, B. Cui, X. Wang, Y. Cao, L. Gao, S. Guo and C. M. Chen, *CrystEngComm*, 2019, **21**, 1750–1757.
31 J. Hu, S. Weng, Z. Zheng, Z. Pei, M. Huang and P. Liu, *J. Hazard. Mater.*, 2014, **264**, 293–302.
32 A. Dehghan, M. H. Dehghani, R. Nabizadeh, N. Ramezanian, M. Alimohammadi and A. A. Najafpoor, *Chem. Eng. Res. Des.*, 2018, **129**, 217–230.
33 S. Q. Guo, X. H. Zhu, H. J. Zhang, B. C. Gu, W. Chen, L. Liu and P. J. Alvarez, *Environ. Sci. Technol.*, 2018, **52**, 6872–6880.
34 Y. Xu, X. Hu, H. Zhu and J. Zhang, *J. Mater. Sci.*, 2016, **51**, 4342–4348.
35 G. J. Lee, Y. C. Zheng and J. J. Wu, *Catal. Today*, 2018, **307**, 197–204.
36 J. Hu, X. Jing, L. Zhai, J. Guo, K. Lu and L. Mao, *Chemosphere*, 2019, **220**, 77–85.
37 Z. Song, X. Dong, N. Wang, L. Zhu, Z. Luo, J. Fang and C. Xiong, *Chem. Eng. J.*, 2017, **317**, 925–934.
38 D. Zhang, L. Chen, C. Xiao, J. Feng, L. Liao, Z. Wang and T. Wei, *J. Nanomater.*, 2016, **2016**, 5697672.

39 Q. L. Yuan, Y. Zhang, H. Y. Yin, Q. L. Nie and W. W. Wu, *J. Exp. Nanosci.*, 2016, **11**, 359–369.
40 R. Li, X. Gao, C. Fan, X. Zhang, Y. Wang and Y. Wang, *Appl. Surf. Sci.*, 2015, **355**, 1075–1082.
41 J. Lu, J. Wu, W. Xu, H. Cheng, X. Qi, Q. Li, Y. Zhang, Y. Guan, Y. Ling and Z. Zhang, *Mater. Lett.*, 2018, **219**, 260–264.
42 J. C. Ahern, R. Fairchild, J. S. Thomas, J. Carr and H. H. Patterson, *Appl. Catal., B*, 2015, **179**, 229–238.
43 A. Zhang, W. Xing, D. Zhang, H. Wang, G. Chen and J. Xiang, *Catal. Commun.*, 2016, **87**, 57–61.
44 H. Huang, X. Li, X. Han, N. Tian, Y. Zhang and T. Zhang, *Phys. Chem. Chem. Phys.*, 2015, **17**, 3673–3679.
45 L. Wang, J. Shang, W. Hao, S. Jiang, S. Huang, T. Wang, Z. Sun, Y. Du, S. Dou, T. Xie, D. Wang and J. Wang, *Sci. Rep.*, 2014, **4**, 7384.
46 Z. Xu, *Ferroelectrics*, 2018, **527**, 37–43.
47 Z. Wang, Z. Chu, C. Dong, Z. Wang, S. Yao, H. Gao, Z. Liu, Y. Liu, B. Yang and H. Zhang, *ACS Appl. Nano Mater.*, 2020, **3**, 1981–1991.
48 P. Intaphong, A. Phuruangrat, S. Thongtem and T. Thongtem, *Mater. Lett.*, 2018, **213**, 88–91.
49 J. M. Montoya-Zamora, A. Martínez-de la Cruz and E. L. Cuéllar, *Res. Chem. Intermed.*, 2017, **43**, 2545–2563.
50 Y. Miao, Z. Lian, Y. Huo and H. Li, *Chin. J. Catal.*, 2018, **39**, 1411–1417.
51 Z. Chen, J. Zeng, J. Di, D. Zhao, M. Ji, J. Xia and H. Li, *Green Energy Environ.*, 2017, **2**, 124–133.
52 M. Gao, D. Zhang, X. Pu, H. Li, J. Li, X. Shao and K. Ding, *Mater. Lett.*, 2015, **140**, 31–34.
53 V. J. Babu, M. Sireesha, R. S. R. Bhavatharini and S. Ramakrishna, *Mater. Lett.*, 2016, **169**, 50–53.
54 H. Yu, H. Huang, K. Xu, W. Hao, Y. Guo, S. Wang, X. Shen, S. Pan and Y. Zhang, *ACS Sustainable Chem. Eng.*, 2017, **5**, 10499–10508.
55 Y. Long, Q. Han, Z. Yang, Y. Ai, S. Sun, Y. Wang, Q. Liang and M. Ding, *J. Mater. Chem. A*, 2018, **6**, 13005–13011.
56 X. C. Song, Y. F. Zheng, H. Y. Yin, J. N. Liu and X. D. Ruan, *New J. Chem.*, 2016, **40**, 130–135.
57 C. Yu, H. He, Q. Fan, W. Xie, Z. Liu and H. Ji, *Sci. Total Environ.*, 2019, **694**, 133727.
58 Z. Liu, J. Liu, H. Wang, G. Cao and J. Niu, *J. Colloid Interface Sci.*, 2016, **463**, 324–331.
59 M. M. Obeid, C. Stampfl, A. Bafekry, Z. Guan, H. R. Jappor, C. V. Nguyen, M. Naseri, D. M. Hoat, N. N. Hieu, A. E. Krauklis, T. V. Vu and D. Gogova, *Phys. Chem. Chem. Phys.*, 2020, **22**, 15354–15364.
60 L. Zeng, F. Zhe, Y. Wang, Q. Zhang, X. Zhao, X. Hu, Y. Wu and Y. He, *J. Colloid Interface Sci.*, 2019, **539**, 563–574.
61 S. Qu, Y. Xiong and J. Zhang, *J. Colloid Interface Sci.*, 2018, **527**, 78–86.
62 G. Jiang, X. Li, Z. Wei, T. Jiang, X. Du and W. Chen, *Powder Technol.*, 2014, **260**, 84–89.
63 J. Shang, T. Chen, X. Wang, L. Sun and Q. Su, *Chem. Phys. Lett.*, 2018, **706**, 483–487.
64 Z. Jiang, Y. Liu, T. Jing, B. Huang, Z. Wang, X. Zhang, X. Qin and Y. Dai, *RSC Adv.*, 2015, **5**, 47261–47264.
65 C. Y. Wang, Q. Zeng and G. Zhu, *Chemosphere*, 2021, **268**, 128854.
66 L. Zhang, F. Liu, X. Xiao, X. Zuo and J. Nan, *Environ. Sci. Pollut. Res.*, 2019, **26**, 28871–28883.
67 J. Zhang, K. Zhu, Y. Zhu, C. Qin, L. Liu, D. Liu, Y. Wang, W. Gan, X. Fu and H. Hao, *Chem. Phys. Lett.*, 2020, **750**, 137483.
68 W. T. Li, W. Z. Huang, H. Zhou, H. Y. Yin, Y. F. Zheng and X. C. Song, *J. Alloys Compd.*, 2015, **638**, 148–154.
69 J. Guo, X. Liao, M. H. Lee, G. Hyett, C. C. Huang, D. W. Hewak, S. Mailis, W. Zhou and Z. Jiang, *Appl. Catal., B*, 2019, **243**, 502–512.
70 F. Xie, X. Mao, C. Fan and Y. Wang, *Mater. Sci. Semicond. Process.*, 2014, **27**, 380–389.
71 H. Li, Z. Yang, J. Zhang, Y. Huang, H. Ji and Y. Tong, *Appl. Surf. Sci.*, 2017, **423**, 1188–1197.
72 J. Liu, D. Li, R. Li, Y. Wang, Y. Wang and C. Fan, *Chem. Eng. J.*, 2020, **395**, 123954.
73 C. Y. Wang, Y. J. Zhang, W. K. Wang, D. N. Pei, G. X. Huang, J. J. Chen, X. Zhang and H. Q. Yu, *Appl. Catal., B*, 2018, **221**, 320–328.
74 X. Zhong, K. X. Zhang, D. Wu, X. Y. Ye, W. Huang and B. X. Zhou, *Chem. Eng. J.*, 2020, **383**, 123148.
75 F. Liu, J. Liang, L. Chen, M. Tong and W. Liu, *J. Mol. Liq.*, 2019, **275**, 807–814.
76 J. Cao, J. Li, W. Chu and W. Cen, *Chem. Eng. J.*, 2020, **400**, 125813.
77 B. Pare, B. Sarwan and S. B. Jonnalagadda, *Appl. Surf. Sci.*, 2011, **258**, 247–253.
78 R. Zhao, X. Li, K. Lin and X. Gao, *Res. Chem. Intermed.*, 2016, **42**, 7031–7043.
79 F. Mokhtari and N. Tahmasebi, *J. Phys. Chem. Solids*, 2021, **149**, 109804.
80 Z. Wei, X. Dong, N. Zheng, Y. Wang, X. Zhang and H. Ma, *J. Mater. Sci.*, 2020, **55**, 16522–16532.
81 H. Yu, D. Ge, Y. Wang, S. Zhu, X. Wang, M. Huo and Y. Lu, *J. Alloys Compd.*, 2019, **786**, 155–162.
82 R. Adhikari, G. Gyawali, S. H. Cho, R. Narro-García, T. Sekino and S. W. Lee, *J. Solid State Chem.*, 2014, **209**, 74–81.
83 K. Xu, X. Fu and Z. Peng, *Mater. Res. Bull.*, 2018, **98**, 103–110.
84 S. Yin, W. Fan, J. Di, T. Wu, J. Yan, M. He, J. Xia and H. Li, *Colloids Surf., A*, 2017, **513**, 160–167.
85 M. Hu, A. Yan, X. Wang, F. Huang, Q. Cui, F. Li and J. Huang, *Mater. Res. Bull.*, 2019, **116**, 89–97.
86 S. Zhong, X. Wang, Y. Wang, F. Zhou, J. Li, S. Liang and C. Li, *J. Alloys Compd.*, 2020, **843**, 155598.
87 L. Zhang, Z. Ma, H. Xu, R. Xie, Y. Zhong, X. Sui, B. Wang and Z. Mao, *Solid State Sci.*, 2018, **75**, 45–52.
88 J. H. Peng, Y. J. Zhao, Q. Ul Hassan, H. Y. Li, Y. B. Liu, S. H. Ma, D. L. Mao, H. Q. Li, L. C. Meng and M. Hojamberdiev, *Adv. Powder Technol.*, 2018, **29**, 1158–1166.
89 Y. He, J. Li, K. Li, M. Sun, C. Yuan, R. Chen, J. Sheng, G. Leng and F. Dong, *Chin. J. Catal.*, 2020, **41**, 1430–1438.

90 Y. Guo, C. H. Lay, D. Zhou, S. Dong, J. Zhang and N. Ren, *Environ. Sci. Pollut. Res.*, 2020, **27**, 17516–17529.
91 K. LópezVelázquez, J. L. Guzmán-Mar, A. Hernández-Ramírez, E. González-Juárez and M. Villanueva-Rodríguez, *Mater. Sci. Semicond. Process.*, 2021, **123**, 105499.
92 M. Nussbaum, N. Shaham-Waldmann and Y. Paz, *J. Photochem. Photobiol., A*, 2014, **290**, 11–21.
93 N. Yu, Y. Chen, W. Zhang, M. Wen, L. Zhang and Z. Chen, *Mater. Lett.*, 2016, **179**, 154–157.
94 S. Niu, R. Zhang, X. Zhou, X. Zhao, H. Suo, Y. Jiao, H. Yao and C. Guo, *Dyes Pigm.*, 2018, **149**, 462–469.
95 S. Wu, W. Sun, J. Sun, Z. D. Hood, S. Z. Yang, L. Sun, P. R. C. Kent and M. F. Chisholm, *Chem. Mater.*, 2018, **30**, 5128–5136.
96 Z. Wei, R. Li and R. Wang, *RSC Adv.*, 2018, **8**, 7956–7962.
97 S. R. Zhu, Q. Qi, Y. Fang, W. N. Zhao, M. K. Wu and L. Han, *Cryst. Growth Des.*, 2018, **18**, 883–891.
98 J. D. Xiao and H. L. Jiang, *Acc. Chem. Res.*, 2019, **52**, 356–366.
99 H. Yang, M. Zhao, J. Zhang, J. Ma, P. Wu, W. Liu and L. Wen, *J. Mater. Chem. A*, 2019, **7**, 20742–20749.
100 W. Jiang, Z. Li, C. Liu, D. Wang, G. Yan, B. Liu and G. Che, *J. Alloys Compd.*, 2021, **854**, 157166.
101 J. Di, S. Li, Z. Zhao, Y. Huang, Y. Jia and H. Zheng, *Chem. Eng. J.*, 2015, **281**, 60–68.
102 S. Li, S. Hu, K. Xu, W. Jiang, J. Liu and Z. Wang, *Nanomaterials*, 2017, **7**, 22.
103 D. Ma, J. Zhong, J. Li, L. Wang and R. Peng, *Appl. Surf. Sci.*, 2018, **443**, 497–505.
104 D. Ma, X. Tang, X. Liu, M. Zhao, R. Peng, J. Li, J. Zhong and R. Duan, *Mater. Res. Bull.*, 2019, **118**, 110521.
105 Y. Shirota and H. Kageyama, *Chem. Rev.*, 2007, **107**, 953–1010.
106 F. Dong, T. Xiong, Y. Sun, Z. Zhao, Y. Zhou, X. Feng and Z. Wu, *Chem. Commun.*, 2014, **50**, 10386–10389.
107 Y. Yu, C. Cao, H. Liu, P. Li, F. Wei, Y. Jiang and W. Song, *J. Mater. Chem. A*, 2014, **2**, 1677–1681.
108 F. Dong, T. Xiong, S. Yan, H. Wang, Y. Sun, Y. Zhang, H. Huang and Z. Wu, *J. Catal.*, 2016, **344**, 401–410.
109 H. Wang, W. Zhang, X. Li, J. Li, W. Cen, Q. Li and F. Dong, *Appl. Catal., B*, 2018, **225**, 218–227.
110 H. Ma, M. Zhao, H. Xing, Y. Fu, X. Zhang and X. Dong, *J. Mater. Sci.: Mater. Electron.*, 2015, **26**, 10002–10011.
111 X. Zhang, G. Ji, Y. Liu, X. Zhou, Y. Zhu, D. Shi, P. Zhang, X. Cao and B. Wang, *Phys. Chem. Chem. Phys.*, 2015, **17**, 8078–8086.
112 F. Cao, J. Wang, Y. Wang, J. Zhou, S. Li, G. Qin and W. Fan, *Nanoscale Adv.*, 2019, **1**, 1124–1129.
113 H. Yu, C. Cao, X. Wang and J. Yu, *J. Phys. Chem. C*, 2017, **121**, 13191–13201.
114 Y. Huang, H. Xu, D. Luo, Y. Zhao, Y. Fang, Y. Wei, L. Fan and J. Wu, *Solid State Sci.*, 2019, **89**, 74–84.
115 X. Meng, Z. Li and Z. Zhang, *Mater. Res. Bull.*, 2018, **99**, 471–478.
116 B. Li, L. Shao, R. Wang, X. Dong, F. Zhao, P. Gao and Z. Li, *J. Mater. Chem. A*, 2018, **6**, 6344–6355.
117 C. Yu, F. Cao, G. Li, R. Wei, J. C. Yu, R. Jin and Q. Fan, *Sep. Purif. Technol.*, 2013, **120**, 110–122.
118 C. Tian, S. Luo, J. She, Y. Qing, N. Yan, Y. Wu and Z. Liu, *Appl. Surf. Sci.*, 2019, **464**, 606–615.
119 Y. Wang, Q. Yang, X. Wang, J. Yang, Y. Dai, Y. He, W. Chen and W. Zhang, *Mater. Sci. Eng., B*, 2019, **244**, 12–22.
120 D. S. Dhawale, R. R. Salunkhe, V. S. Jamadade, D. P. Dubal, S. M. Pawar and C. D. Lokhande, *Curr. Appl. Phys.*, 2010, **10**, 904–909.
121 C. Yan, Z. Zhang, W. Wang, T. Ju, H. She and Q. Wang, *J. Mater. Sci.: Mater. Electron.*, 2018, **29**, 18343–18351.
122 J. Xu, Y. Hu, C. Zeng, Y. Zhang and H. Huang, *J. Colloid Interface Sci.*, 2017, **505**, 719–727.
123 S. Cui, G. Shan and L. Zhu, *Appl. Catal., B*, 2017, **219**, 249–258.
124 B. Ge, L. Han, X. Liang, F. Li, X. Pu, X. Zhu, Z. Zhang, X. Shao, C. Jin and W. Li, *Appl. Surf. Sci.*, 2018, **462**, 583–589.
125 C. J. Chang, P. Y. Chao and K. S. Lin, *Appl. Surf. Sci.*, 2019, **494**, 492–500.
126 Z. Cui, H. Song, S. Ge, W. He and Y. Liu, *Appl. Surf. Sci.*, 2019, **467–468**, 505–513.
127 J. Zhang, J. Lv, K. Dai, C. Liang and Q. Liu, *Appl. Surf. Sci.*, 2018, **430**, 639–646.
128 C. Zhao, Y. Liang, W. Li, X. Chen, Y. Tian, D. Yin and Q. Zhang, *J. Mater. Sci.: Mater. Electron.*, 2020, **31**, 1868–1878.
129 J. Li, Q. Zhou, F. Yang, L. Wu, W. Li, R. Ren and Y. Lv, *New J. Chem.*, 2019, **43**, 14829–14840.
130 T. Jiang, J. Li, Y. Gao, L. Li, T. Lu and L. Pan, *J. Colloid Interface Sci.*, 2017, **490**, 812–818.
131 J. Zhang, J. Xia, S. Yin, H. Li, H. Xu, M. He, L. Huang and Q. Zhang, *Colloids Surf., A*, 2013, **420**, 89–95.
132 C. Yang, J. Zhong, J. Li, S. Huang and R. Duan, *Mater. Lett.*, 2020, **259**, 126766.
133 H. Liu, C. Yang, J. Huang, J. Chen, J. Zhong and J. Li, *Chem. Commun.*, 2020, **113**, 107806.
134 X. Sun, J. Lu, J. Wu, D. Guan, Q. Liu and N. Yan, *J. Colloid Interface Sci.*, 2019, **546**, 32–42.
135 F. Dong, Y. Sun, M. Fu, Z. Wu and S. C. Lee, *J. Hazard. Mater.*, 2012, **219–220**, 26–34.
136 S. Zhang and J. Yang, *Ind. Eng. Chem. Res.*, 2015, **54**, 9913–9919.
137 X. Jia, J. Cao, H. Lin, M. Zhang, X. Guo and S. Chen, *Appl. Catal., B*, 2017, **204**, 505–514.
138 H. Lin, H. Ye, X. Li, J. Cao and S. Chen, *Ceram. Int.*, 2014, **40**, 9743–9750.
139 T. S. Jamil, E. S. Mansor and R. A. Nasr, *Desalin. Water Treat.*, 2016, **57**, 14750–14761.
140 Y. Bai, X. Shi, P. Wang, L. Wnag, K. Zhang, Y. Zhou, H. Xie, J. Wang and L. Ye, *Chem. Eng. J.*, 2019, **356**, 34–42.
141 S. H. Li, N. Zhang, X. Xie, R. Luque and Y. J. Xu, *Angew. Chem., Int. Ed.*, 2018, **57**, 13082–13085.
142 G. Liu, H. Xu, D. Li, Z. Zou, Q. Li and D. Xia, *Eur. J. Inorg. Chem.*, 2019, **2019**, 4887–4893.
143 X. Shi, P. Wang, W. Li, Y. Bai, H. Xie, Y. Zhou and L. Ye, *Appl. Catal., B*, 2019, **243**, 322–329.
144 G. Wang, X. Luo, Y. Huang, A. Kuang, H. Yuan and H. Chen, *RSC Adv.*, 2016, **6**, 91508–91516.

145 J. Di, J. Xia, Y. Ge, H. Li, H. Ji, H. Xu, Q. Zhang, H. Li and M. Li, *Appl. Catal., B*, 2015, **168–169**, 51–61.
146 C. Zhao, Y. Liang, W. Li, Y. Tian, X. Chen, D. Yin and Q. Zhang, *RSC Adv.*, 2017, **7**, 52614–52620.
147 X. Su, J. Yang, X. Yu, Y. Zhu and Y. Zhang, *Appl. Surf. Sci.*, 2018, **433**, 502–512.
148 M. Du, Y. Du, Y. Feng, Z. Li, J. Wang and N. Jiang, *Cellulose*, 2019, **26**, 5543–5557.
149 L. Ren, D. Zhang, X. Hao, X. Xiao, Y. Jiang, J. Gong, F. Zhang, X. Zhang and Z. Tong, *Mater. Res. Bull.*, 2017, **94**, 183–189.
150 Y. Wang, Y. Long, Z. Yang and D. Zhang, *J. Hazard. Mater.*, 2018, **351**, 11–19.
151 X. Xiao, C. Zheng, M. Lu, L. Zhang, F. Liu, X. Zuo and J. Nan, *Appl. Catal., B*, 2018, **228**, 142–151.
152 C. Y. Wang, X. Zhang, H. B. Qiu, W. K. Wang, G. X. Huang, J. Jiang and H. Q. Yu, *Appl. Catal., B*, 2017, **200**, 659–665.
153 R. Li, J. Liu, X. Zhang, Y. Wang, Y. Wang, C. Zhang, X. Zhang and C. Fan, *Chem. Eng. J.*, 2018, **339**, 42–50.
154 Y. Bai, L. Ye, T. Chen, L. Wang, X. Shi, X. Zhang and D. Chen, *ACS Appl. Mater. Interfaces*, 2016, **8**, 27661–27668.
155 C. Y. Wang, X. Zhang, X. N. Song, W. K. Wang and H. Q. Yu, *ACS Appl. Mater. Interfaces*, 2016, **8**, 5320–5326.
156 G. Gupta and S. K. Kansal, *Process Saf. Environ.*, 2019, **128**, 342–352.
157 M. Shabani, M. Haghighi and D. Kahforoushan, *J. Cleaner Prod.*, 2019, **207**, 444–457.
158 X. Liu, X. Jiang, Z. Chen, J. Yu and Y. He, *Mater. Lett.*, 2018, **210**, 194–198.
159 L. Wang, X. Min, X. Sui, J. Chen and Y. Wang, *J. Colloid Interface Sci.*, 2020, **560**, 21–33.
160 S. Heidari, M. Haghighi and M. Shabani, *J. Cleaner Prod.*, 2020, **259**, 120679.
161 S. Meng, Y. Bi, T. Yan, Y. Zhang, T. Wu, Y. Shao and D. Wei, *J. Hazard. Mater.*, 2018, **358**, 20–32.
162 D. Du, W. Li, S. Chen, T. Yan, J. You and D. Kong, *New J. Chem.*, 2015, **39**, 3129–3136.
163 H. Y. Xu, X. Han, Q. Tan, K. J. Wu and S. Y. Qi, *Front. Mater. Sci.*, 2017, **11**, 120–129.
164 W. J. Kim, D. Pradhan, B. K. Min and Y. Sohn, *Appl. Catal., B*, 2014, **147**, 711–725.